A Multifunctional Patch for Minimally Invasive Tissue Sealing: Design Strategies and Applications

by

Sarah J. Wu

B.S. Mechanical Engineering, Massachusetts Institute of Technology, 2019

Submitted to the Department of Mechanical Engineering
in partial fulfillment of the requirements for the degree of
Master of Science in Mechanical Engineering

at the

MASSACHUSETTS INSTITUTE OF TECHNOLOGY

June 2021

Author……
Department of Mechanical Engineering
May 13, 2021

Certified by……
Xuanhe Zhao
Professor of Mechanical Engineering
Thesis Supervisor

Accepted by……...……
Nicolas Hadjiconstantinou
Professor of Mechanical Engineering
Chairman, Department Committee on Graduate Theses

A Multifunctional Patch for Minimally Invasive Tissue Sealing: Design Strategies and Applications

by
Sarah J. Wu

Submitted to the Department of Mechanical Engineering on
May 13, 2021 in partial fulfillment of the requirements for the
degree of Master of Science in Mechanical Engineering

Abstract

Bioadhesive materials have garnered great attention due to their potential to replace sutures and staples during surgical procedures. Compared to the traditional mechanical sealing modalities, bioadhesive materials are generally associated with short application times and reduced tissue damage. However, the complexities of delivering bioadhesive materials through narrow spaces and achieving strong adhesion in fluid-rich physiological environments continue to present substantial limitations to the broader surgical translation of existing glues and sealants, particularly in the domain of minimally invasive surgery. This thesis presents the design and testing of a surgically implantable tissue-sealing patch for versatile minimally invasive wound-closing applications. The design approach is guided by the clinical needs to resist contamination caused by pre-exposure body fluids, achieve fast, strong, and fluid-tight tissue adhesion, and prevent postsurgical biofouling and inflammation. These criteria are realized through the synergistic integration of multiple distinct functional layers, including (*1*) a microtextured bioadhesive layer comprised of an interpenetrating NHS-grafted PAAc and biopolymer network, (*2*) a blood-repellent hydrophobic fluid layer infused into the microtextured bioadhesive layer, and (*3*) an antifouling zwitterionic polymer-interpenetrated elastomer backing. Strategies guiding the design and characterization of each layer are discussed, and tailored form factors for specific minimally invasive clinical applications are further demonstrated. This platform provides a basis for the future design of multifunctional, antifouling, and bioadhesive materials.

Thesis supervisor: Xuanhe Zhao
Title: Professor of Mechanical Engineering

Acknowledgements

First and foremost, I would like to thank my thesis advisor, Prof. Xuanhe Zhao, who has been a constant source of support and inspiration over the past year and a half. I feel extremely fortunate to be working with somebody who has so much knowledge to share, encourages creativity, and always asks the right questions. I am also grateful for Dr. Christoph Nabzdyk, who has guided much of this research and has tirelessly provided me with insightful comments (even after late nights in the ICU).

I also owe a debt of gratitude to Hyunwoo Yuk, who has been teaching me new things since the first day I stepped foot in the lab. I will dearly miss being bench neighbors and enjoying discussions about the latest papers, receiving life advice, and learning interesting rabbit facts. Without him, I could not have completed this work.

Everyone in the SAMS lab group deserves a special thanks for their support and friendship. Heejung has been the best lab buddy I could ask for, and never fails to make me laugh. I'll always enjoy the hours I spend in the surgery room with Jingjing, the rat Queen. Shaoting, Xinyue, Tao, Jue, Jiahua, Liu, Xiaoyu, and Yoonho: I am constantly inspired by all of your work ethic and creativity, and I'm thankful to have so many role models to look up to here. Heather, I hope to continue our long-distance Zoom study sessions. I am immensely appreciative of Xinyu, who helped me assimilate to graduate school during my first semester. And of course, thank you to Christina for being awesome and making everything possible by taking care of our administrative tasks.

I have so much love and gratitude for my parents. My dad is always there to "transfer brain power" and lend me wisdom when I need advice. My mom is my confidant and my biggest supporter. Without their shipments of snacks and ramen noodles, I'm not sure where I would be.

Last but not least, I am grateful for my roommate Irene and my sister Chloe, who have kept me sane through a global pandemic and whose friendship is more meaningful to me than I can possibly put into words here. To Chloe, thank you for being my lifelong best friend and inspiring me in so many ways.

Contents

CHAPTER 3: CHARACTERIZATION: METHODS AND RESULTS

List of Figures

List of Tables

CHAPTER 1

Introduction

1.1 Clinical Motivation

The ability to connect tissues is one of the cornerstones of general surgery. To this end, the traditional strategies of applying mechanical fasteners (i.e., sutures and staples) remain the current standards for sealing and repairing tissues in both open and minimally invasive surgery. However, these modalities carry inherent drawbacks. Suturing entails complex manipulations which are time-consuming and require a high level of surgical skill, and is therefore disadvantageous during time-sensitive or anatomically challenging operations. Surgical staples, while comparatively simpler to apply, have been associated with a rising number of adverse events caused by complications such as staple malformations and stapler misfirings [1]–[3]. Moreover, both sutures and staples achieve mechanical seals via pointwise punctures through tissue, which can be mechanically damaging and are prone to dehiscence, leakage, and inflammation [4]. Associated postoperative complications, such as anastomotic leaks and fibrous adhesion formation with surrounding organs, can result in devastating clinical consequences for patients and often require subsequent readmission surgeries to achieve definitive surgical repair [5]–[8].

The challenges associated with sutures and staples are further amplified in minimally invasive settings, during which the use of endoscopic equipment typically limits visualization, depth perception, range of motion, and haptic feedback [2], [9]–[12]. At the same time, the demand for adopting minimally invasive and robotic surgical techniques has steadily trended upward due

to substantial associated improvements in patient outcomes such as reductions in blood loss, operation and recovery times, and healthcare costs [13], [14]. As such, there remains an unmet need for tissue sealing methods which can overcome the functional challenges for minimally invasive and robotic delivery [15].

1.2 TISSUE ADHESIVES: OVERVIEW AND LIMITATIONS

Tissue adhesives, commonly in the form of liquid glues and sealants, present attractive features as alternatives or adjuncts to sutures and staples for hemostasis, tissue sealing, and delivery of drugs and biologics [4], [16]–[28]. These materials generally carry the benefits of having short application times and inflicting minimal tissue trauma. Additionally, the continuous nature of their adhesive seals, rather than pointwise punctures, may reduce the incidence of suture/staple line leaks and their associated complications. Tissue adhesives therefore hold great potential for minimally invasive applications in which delicate tissues and difficult-to-access defect locations can be prohibitive to the use of sutures and staples.

Despite these advantages, the practical applications of existing tissue adhesives are limited by shortcomings related to their delivery method, adhesion strength, and/or tissue interaction (**Figure 1-1** and **Table 1-1**). For instance, most commercially-available bioadhesives take the form of liquid glues, which are prone to displacement or dilution in dynamic and moist physiological environments. Additionally, many bioadhesive materials struggle to adhere in the presence of body fluids, which can compromise bonding groups in the material (e.g., by hydrolysis) and prevent adhesion to the target tissue [29]. To offer greater control over polymerization, several bioadhesives have been reported which incorporate external-stimuli-based adhesion activation

such as ultraviolet (UV) light crosslinking [27], [30]. However, the need for external activation sources can hinder their ease of use by introducing additional application steps and equipment. As a consequence of these limitations, many of the existing tissue adhesives are associated with slow adhesion processes and relatively low adhesion strength [19]. The mechanical properties of the tissue adhesives are important considerations as well. For example, fibrin- and PEG-based sealants exhibit low cohesive strength and are therefore nonideal for applications which involve high or dynamic mechanical loading. On the other hand, materials which solidify into rigid polymers, such as cyanoacrylates, are also undesirable due to the resulting adhesive-to-host compliance mismatch and associated stress concentration at the interface [16]. These stiff materials can incite excessive scar tissue formation. Additional clinical concerns include inflammatory responses, such as postoperative adhesion formation, and perioperative infectious complications [7], [21], [23]. In particular, postoperative adhesions represent major clinical complications following pericardial, abdominal, and intrauterine surgery. Characterized by fibrous bands of scar tissue creating abnormal seams between organ surfaces, adhesions can lead to loss of tissue function and often require substantial surgical reintervention (i.e., adhesiolysis procedures). With this risk in mind, an ideal bioadhesive should prevent, rather than promote, adhesion to the tissue surrounding the wound site. A brief summary of relevant tissue adhesive technologies and their corresponding functional performance for surgical application are displayed in **Table 1-1**.

1.3 THE SCOPE OF THE THESIS

The goal of this thesis is to present a design strategy for a multifunctional tissue sealing patch guided by the functional demands of minimally invasive surgery. The specific aims of the proposed platform are summarized as follows:

1. To achieve fast, strong adhesion to wet tissue surfaces;
2. To resist contamination by body fluids;
3. To mitigate postoperative inflammatory and infectious complications;
4. To undergo facile delivery and application using minimally invasive surgical instruments.

Section 2 will describe the design of the multifunctional patch and the mechanisms for achieving each of the specific aims. In Section 3, methods to characterize the performance of the patch will be presented and experimental results will be discussed. Section 4 will propose several strategies for delivering the patch in a range of minimally invasive applications, including proof-of-concept *ex vivo* porcine demonstrations. Finally, Section 5 will discuss the takeaways and future outlook of the work.

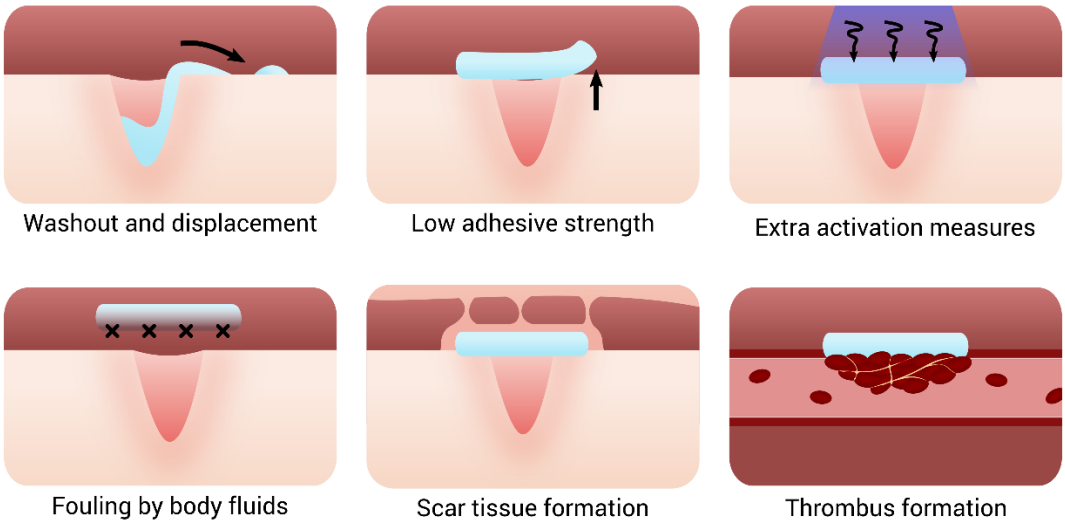

Figure 1-1: Common functional limitations of tissue adhesives.

Table 1-1: Comparison of various tissue adhesives and their functional performance for surgical application.

Material & Form	Wet Tissue Adhesion	Body Fluid Resistance	Adhesion Speed	Adhesion Performance	Antifouling	MI Delivery & Application	Reference
Fibrin liquid glue	No	No	Slow (>3 min)	Low	No	Yes (injection)	FDA-approved product (Tisseel)
PEG liquid glue	No	No	Slow (>2 min)	Low	No	Yes (injection)	FDA-approved product (Coseal)
Cyanoacrylate liquid glue	No	No	Fast (<1 min)	High	No	N/R	FDA-approved product (Histoacryl)
Mussel-inspired adhesives	Yes	Yes	Very Slow (>15 min)	Intermediate	No	Yes (Injection)	*24, 25*
Bulk tough hydrogel	Yes	Yes	Slow (>3 min)	High	No	No	*26*
Hydrophobic liquid glue	Yes	Yes	Slow (>2 min)	Intermediate	No	Yes (UV curing)	*27*
GelMA liquid glue	No	No	Slow (>2 min)	Intermediate	No	Yes (UV curing)	*28*
Double-sided tape	Yes	No	Fast (> 5 sec)	High	No	No	*18*

CHAPTER 2

Design of the Multifunctional Patch

2.1 OVERVIEW

The ideal characteristics of a bioadhesive material are defined by a comprehensive set of clinical requirements. Optimally, a bioadhesive should be capable of achieving robust adhesion to biological tissues in wet environments, form hermitic (fluid-tight) seals, possess mechanical properties compatible with the underlying tissue substrate, exhibit good biocompatibility and biodegradability, and have low levels of inflammation as well as a minimal risk of infection.

To develop an effective tissue sealant based on the requirements listed above, we propose the design of a solid patch featuring multiple functional layers: (*1*) a bioadhesive substrate, (*2*) a protective hydrophobic matrix, and (*3*) an antifouling non-adhesive backing (**Figure 2-1**). Through the synergistic integration of three components possessing distinct material and structural properties, the patch can be tuned to optimize its performance for a wide range of functionality with fewer practical trade-offs and limitations compared to single-material systems. In the following sections of this chapter, the mechanisms and fabrication methods of each layer will be described.

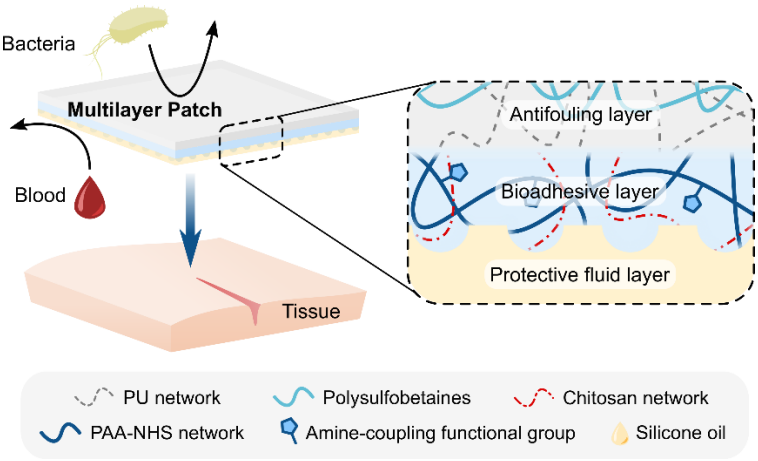

Figure 2-1: Illustrated schematic of the multilayer bioadhesive patch. The patch comprises a textured bioadhesive fused with an antifouling polymer layer on the non-adherent side, and is wetted with a hydrophobic fluid layer on the adherent side to repel body fluids.

2.2 Design of the Bioadhesive Layer

The bioadhesive layer, positioned in between the two other functional layers, serves as the basis for the patch to achieve robust, fluid-tight seals. Its key function is to form fast adhesion with wet tissue surfaces.

2.2.1 Material Composition

The bioadhesive material system described in this work is a double-network hydrogel comprised of poly(acrylic acid) grafted with *N*-hydroxysuccinimide ester (PAA-NHS ester) and chitosan [15], [19]. Poly(acrylic acid) is a highly hydrophilic polymer which is rich with ionizable

carboxylic acid side chains (**Figure 2-2a**). PAA-based materials are therefore capable of rapidly absorbing water and forming a high density of hydrogen bonds. Grafting of NHS esters to PAA can be carried out using carbodiimide (EDC/NHS) crosslinker chemistry (**Figure 2-3**): first, carboxylic acid groups on PAA react with EDC to form an active intermediate. The unstable intermediate reacts with NHS (or water-soluble Sulfo-NHS) to form an amine-reactive NHS ester, which can later conjugate to primary amines to form a stable amide bond [31]. The NHS ester is sensitive to hydrolysis and should therefore be kept in a dry-stable state to preserve reactivity with amines. Over time, PAA can be degraded via dissolution by hydration.

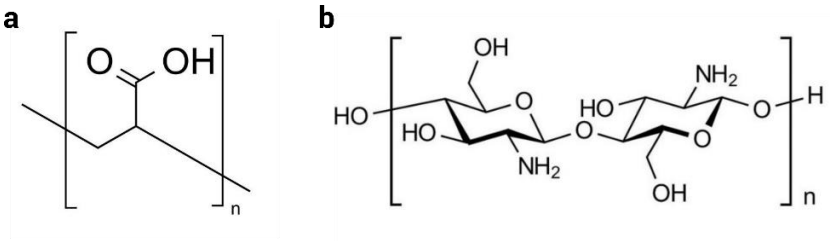

Figure 2-2: Chemical structures of (a) poly(acrylic acid) and (b) chitosan.

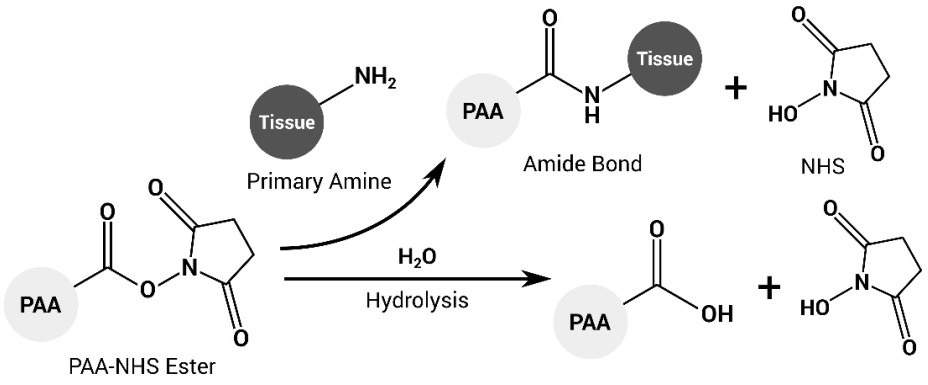

Figure 2-3: PAA-NHS ester reaction scheme for the formation of an amide bond between primary amines in proteins contained on tissue surfaces (upper), and the competing hydrolysis reaction (lower).

The second key component in the bioadhesive material is chitosan, a natural polysaccharide derived from chitin (**Figure 2-2b**) [32], [33]. Chitosan has been employed in a wide variety of biomedical applications, including as microspheres for drug delivery, coatings for orthopedic implants, scaffolds for tissue engineering, and various forms of bioadhesive materials. In addition to exhibiting favorable properties such as biocompatibility, non-toxicity, non-antigenicity, and low reactivity, the chemical structure of chitosan contains cationic amino groups which can form electrostatic interactions with tissue surfaces. Moreover, chitosan can be degraded by enzyme-catalyzed hydrolysis and is thus an excellent candidate for biomedical applications.

Drawing from the advantages of both polymers, the bioadhesive material used in this work is an interpenetrating network (IPN) of PAA-NHS ester and chitosan. The material is prepared via photopolymerization of the precursor solution, which contains the monomers, α-ketoglutaric acid as a photo-initiator, and poly(ethylene glycol dimethacrylate) (PEGDMA) as a biodegradable crosslinking agent. The cured material is fully dried prior to use.

2.2.2 Mechanism of Adhesion

In many clinical scenarios, complete removal of body fluids from tissue surfaces and maintenance of a dry physiological environment is impractical; therefore, the ability to form adhesion with wet tissues is a key property for most tissue adhesives. Conventional tissue adhesives tend to rely on diffusion of their monomers or polymers through the interfacial water to form crosslinks or chemical bonds with the tissue. Consequently, the time to form adhesion is dependent on the diffusion rate of these components, which can take tens of minutes, depending on their molecular weight and chemical features [20].

To reduce the time to form adhesion, the PAA-NHS ester/chitosan network employs a dry-crosslinking mechanism [15], [19]: first, the dry material is brought into contact with the wet tissue surface, and the highly hydrophilic PAA chains lend the material to rapid uptake of the interfacial water. Removal of the interfacial water occurs within seconds, which causes the material to swell (equilibrium water content of around 92% by volume) and quickly form physical crosslinks with the tissue. Owing to the carboxylic acid side chains of PAA, a high density of hydrogen bonds between the material and the tissue can be achieved. Electrostatic interactions between moieties of both PAA and chitosan further contribute to the short-timescale adhesion strength. The second part of the dry-crosslinking mechanism entails formation of covalent amide bonds between the NHS ester groups grafted on PAA and primary amine residues which are abundant on tissue surfaces. This covalent coupling is key to the long-term stable adhesion of the material. Chemical anchorage of the long-chain PAA network to the tissue substrate provides a relatively high work of adhesion [34]. In addition, the swollen PAA/chitosan double network has high stretchability and fracture toughness, which results in an overall high interfacial toughness.

In the present work, the bioadhesive layer is designed to feature a micro-scale surface topography consisting of embedded bioadhesive microparticles (**Figure 2-4)**. Details of the surface structure are described further in Section 2.3. The micro-scale surface structure plays a secondary role in the adhesion strength between the patch and the tissue substrate by contributing mechanical interlocking effects. Mechanical interlocking can enhance adhesion by increasing the contact area between the adhesive and the tissue, as well as by increasing the adhesive failure energy by provoking energy expenditure during crack propagation [35], [36]. Friction between the roughened bioadhesive surface and the tissue substrate during the initial stages of contact and adhesion can also act to prevent sliding and displacement of the adhesive during the adhesion process [37].

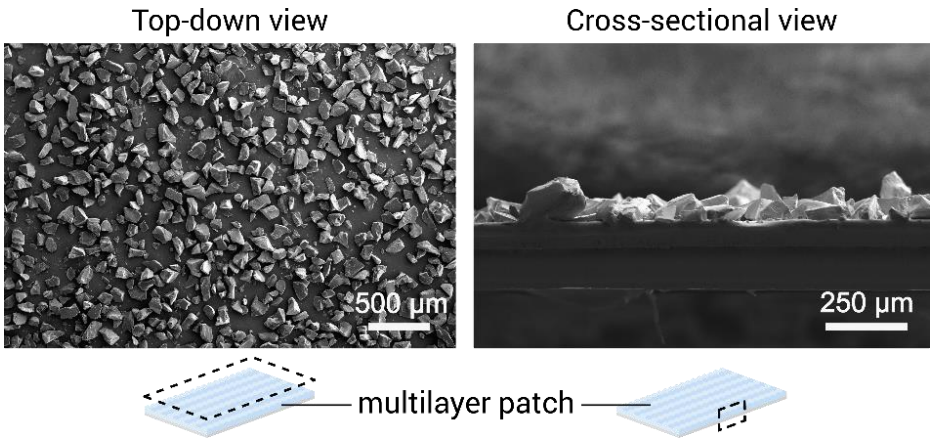

Figure 2-4: Scanning electron micrographs (SEMs) of the microtextured bioadhesive surface from a top-down (left) and cross-sectional (right) point of view. The surface is prepared by embedding cryogenically grinded bioadhesive microparticles prior to complete drying of the substrate. A lubricating fluid is later impinged into the microtopography to form a stable hydrophobic matrix.

2.3 Design of the Hydrophobic Liquid-Infused Matrix

The bioadhesive polymer network described in Section 2.2 can suffer from premature swelling and contamination of the tissue-bonding functional groups if pre-exposed to water, blood, or other body fluids. In order to preserve the adhesive capacity of the bioadhesive material as it is maneuvered through the body, a second layer is introduced: a hydrophobic liquid-infused surface. The liquid-infused surface serves as a protective barrier by repelling blood and other immiscible contaminants until sufficient pressure is applied at the tissue surface to trigger dewetting.

2.3.1 Overview of Liquid-Infused Surfaces

Microtextured (porous) surfaces infiltrated with a lubricating fluid have been reported to show excellent liquid-repellent behavior, with broad applications ranging from anti-icing surfaces to biofilm-resistant catheters and implants [38]–[44]. The basic principle behind liquid-infused surfaces (LIS), also known as slippery liquid-infused porous surfaces (SLIPS), lies in the tethering of a liquid to a surface, stabilized by surface chemistry and topographical effects, which provides a physical barrier to preclude adsorption to and fouling of the solid surface. The design of liquid-infused surfaces draws inspiration from nature: carnivorous *Nepenthes* pitcher plants possess leaves with special surface properties adapted to capture prey [45]. These surfaces feature a highly regular microstructure of ridges projecting from the pitcher wall. When wet, the microstructure is remarkably effective at locking in a slippery fluid layer, so that the pitcher leaf becomes covered by a thin, stable liquid film which causes insects to slide into the digestive region by a process known as aquaplaning. The high wettability of *Nepenthes* leaves is attributed to a combination of hydrophilicity and surface microtopography.

By harnessing design principles similar to those exhibited by the *Nepenthes* pitcher plant, synthetic versions of slippery liquid-infused surfaces can be produced which exhibit superior non-wetting behavior compared to typical solid-phase superhydrophobic surfaces (e.g., those based on the "lotus effect") [39]. The presence of a smooth liquid interface mitigates droplet pinning, allowing immiscible liquids to be repelled without impediment. Liquid-infused surfaces are created by fabricating a solid substrate featuring a nano- or micro-scale topography, which promotes wetting of a lubricating liquid via capillary wicking and increased contact area with the solid. The stability of the liquid-infused surface and its effectiveness in repelling immiscible liquids are governed by interfacial energy relations described in Section 2.3.3.

2.3.2 Selection of the Lubricating Fluid

The liquid infiltrating the microtextured substrate plays a key role in the overall design of the LIS. For the present application, which requires the LIS to maintain stability through the process of being maneuvered within the body, the viscosity of the lubricating fluid is an important parameter. While higher viscosity fluids tend to remain more stably locked into the underlying substrate in dynamic conditions, they also lead to greater frictional forces with immiscible liquids, resulting in a reduction in the repelled droplet velocity [40], [44]. Furthermore, current designs and applications of liquid-infused films typically have the singular aim to maintain the protective overlayer indefinitely; however, in this case, the ultimate fate of the lubricating layer is to be removed from the interface in order to expose the underlying adhesive material for tissue contact. Therefore, the pressure threshold required to squeeze out the interfacial oil should not be excessive, as high forces can potentially cause mechanical damage to the underlying tissue. Careful selection

of the lubricating fluid viscosity is therefore crucial to striking a balance between these desired effects.

The lubricating fluid must also be immiscible with blood and other body fluids, exhibit good chemical affinity with the bioadhesive substrate, and not induce secondary wound contamination or have toxic effects. Requirements related to the interfacial energies of the lubricating fluid are discussed further in Section 2.3.3. Based on these requirements, silicone oil (100 cSt) was selected as the lubricating fluid for the liquid-infused bioadhesive system.

Sterilized silicone oils are routinely used as medical lubricants for minimally invasive devices and implants, and as intraocular tamponades during vitreoretinal surgery [46]. In general, it has been reported that silicone oils with a higher average molecular weight (i.e., higher viscosity oils) exhibit greater biocompatibility due to a lower tendency to emulsify. Silicone oils are commercially-available in a range of viscosities, allowing for systematic optimization of the LIS system. Future iterations of the liquid-infused bioadhesive design may benefit from investigating the performance of naturally-derived oils, such as soybean and vegetable oils, which could provide greater biodegradability.

2.3.3 THERMODYNAMIC CONDITIONS

Smith *et al*. described the fundamental energy relations which govern the morphology of the liquid-substrate contact line [44]. The design of a fluid-repellent liquid-infused surface generally requires consideration of the interactions between four phases present in the system: the lubricant, the ambient air, the liquid to be repelled, and the solid substrate (**Figure 2-5**). In the present work, the corresponding system components are silicone oil, air, contaminating body fluids

(e.g., blood), and the bioadhesive material, respectively. Here, an additional material—the biological tissue—should also be considered for analysis of interactions at the tissue surface. These components will be denoted by subscripts *o* for oil, *b* for blood, *a* for air, *ad* for adhesive, and *t* for tissue.

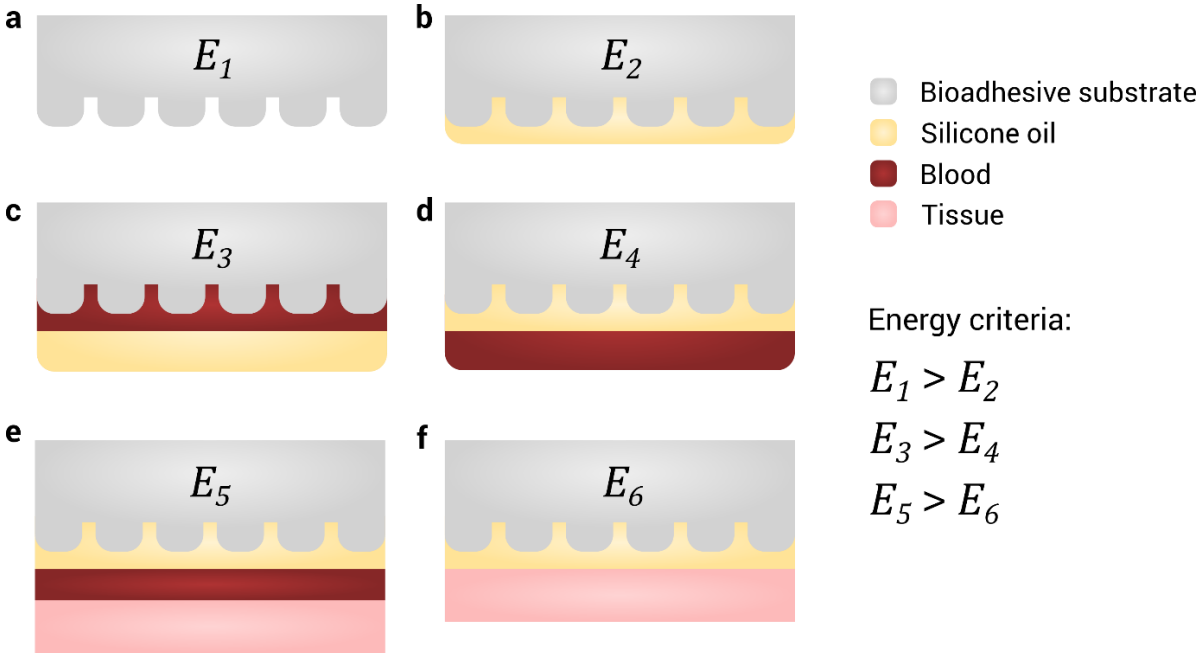

Figure 2-5: Schematics of the wetting configurations for a system comprising air, the bioadhesive substrate, silicone oil, blood, and tissue.

The microparticles embedded in the bioadhesive surface can be treated as a close-packed model of uniform hemispheres with radius R and packing density $D = \pi\sqrt{3}/6$ (i.e., hexagonal packing). The ratio of total surface area to the projected area is $r = \frac{4\pi R^2}{6\sqrt{3}R^2} = \frac{2\pi}{3\sqrt{3}}$.

First, to determine the stable configuration of the liquid-infused bioadhesive in air, we compare the total surface energies (denoted E_n) of two different configurations (*a*, *b*) consisting of

the bioadhesive substrate, the lubricating fluid, and air. For the lubricant to infiltrate the bioadhesive surface, we require:

$$E_1 > E_2 \tag{2.1a}$$

Applying Young's equation, this condition becomes:

$$r\cos\theta_{o/ad(a)} > 1 \tag{2.1b}$$

where $\theta_{o/ad(a)}$ denotes the apparent contact angle of the silicone oil on the adhesive substrate in air.

By a similar treatment, for the bioadhesive surface to be preferentially wetted by the silicone oil in the presence of blood, the energies of configurations *c* and *d* can be compared:

$$E_3 > E_4 \Leftrightarrow \gamma_{o/a}\cos\theta_{o/ad(a)} - \gamma_{b/a}\cos\theta_{b/ad(a)} > 0 \tag{2.2}$$

where $\gamma_{x/y}$ denotes the interfacial energy between substances *x* and *y*.

Finally, we compare the total surface energies of two configurations (*e*, *f*) at the tissue surface to ensure the repulsion of blood by the silicone oil matrix. The corresponding energy relation that must be satisfied is:

$$E_5 > E_6 \Leftrightarrow \gamma_{o/b} + \gamma_{o/a}\cos\theta_{o/t(a)} - \gamma_{b/a}\cos\theta_{b/t(a)} > 0 \tag{2.3}$$

The conditions summarized by Eqns. (2.1)-(2.3) provide a toolkit for designing an effective blood-repellent liquid-infused bioadhesive system. System energies can be approximated by measuring the relevant contact angles, interfacial energies, and geometrical parameters. The values of the parameters for the present system are $\gamma_{o/a}$ = 20.9 mN m^{-1}, $\gamma_{b/a}$ = 72.0 mN m^{-1}, $\gamma_{o/b}$ = 40 mN m^{-1}, $\theta_{o/ad(a)}$ = 4.5°, $\theta_{b/ad(a)}$ = 96°, $\theta_{o/t(a)}$ = 4.2°, $\theta_{b/ad(a)}$ = 84° [47]–[50]. Substitution of these values in to Eqns. (2.1)-(2.3) confirm that the energy criteria for stable oil infiltration and blood repellency at the tissue interface are satisfied.

2.3.4 MICROSCALE TOPOGRAPHY FABRICATION

Some methods for fabricating nano- and micro-scale surface features include chemical and physical etching, molding, layer-by-layer deposition, and chemical coating. However, these methods can be time-consuming or expensive to test design iterations, and/or incompatible for patterning the bioadhesive material. For example, curing and drying the bioadhesive hydrogel in a micropatterned mold results in poor transfer of patterns with small dimensions or high aspect ratios. In this work, the strategy for producing a surface topography with tunable feature lengths is based on cryogenic grinding. In this process, small pieces of the dry bioadhesive material are chilled by liquid nitrogen and finely milled into microparticles. The average size of these bioadhesive microparticles can be tuned by varying the cryogenic grinding frequency. As the grinding frequency is increased, the average size of the microparticles decreases. Further sorting of microparticles by size can be achieved by passing the resulting powder through a series of fine-mesh sieves. For the silicone oil-infused bioadhesive system, it was found that an average microparticle size of <100 μm generates a topography that can imbibe 100 cSt silicone oil, which remains stably adhered in the presence of blood (further details in Section 3.2).

In order to embed the microparticles into the surface of a flat bioadhesive substrate, prepared microparticles are sifted through a fine-mesh sieve over the surface of a bioadhesive hydrogel (after curing, prior to complete drying). Due to the water content of the bioadhesive substrate, the contact points of the microparticles can become hydrated and form crosslinks with the bulk. Application of a gentle flow of nitrogen removes the non-embedded particles, and the entire assembly is thoroughly dried prior to infiltration with silicone oil.

While the microparticle-based surface generation strategy holds numerous advantages such as ease of fabrication, tunable design iteration, and preservation of the material's adhesive

capacity, it results in irregular surface features and poses the risk of microparticle detachment. Future development of the liquid-infused bioadhesive surface could include opportunities to create more controlled, regular patterns through alternative fabrication methods (e.g., 3D printing, embossing, photo-lithographic printing, and surface etching). This could enable topographies of greater complexity to be generated, such as unidirectional patterns for directed fluid repellence. Another promising potential form factor would be a porous mesh structure, which would provide enhanced flexibility and allow for fluids to be discharged through the pores at low pressure thresholds. In-depth discussion of these designs will not be included in the scope of the current thesis.

2.3.5 PRESSURE-TRIGGERED INTERFACIAL DEWETTING

As established in Section 2.3.3, the silicone-oil infused microtextured bioadhesive surface should be designed to achieve thermodynamic stability in the preferred configurations, such that the lubricating fluid layer is maintained during manipulation of the patch through body fluid-rich environments. However, this layer must ultimately be removed from the bioadhesive/tissue interface to allow adhesion to occur (**Figure 2-6**). Dewetting of the textured surface can occur under the influence of externally applied pressure. This section will discuss several features of interested which affect fluid squeeze-out behavior between two solid surfaces.

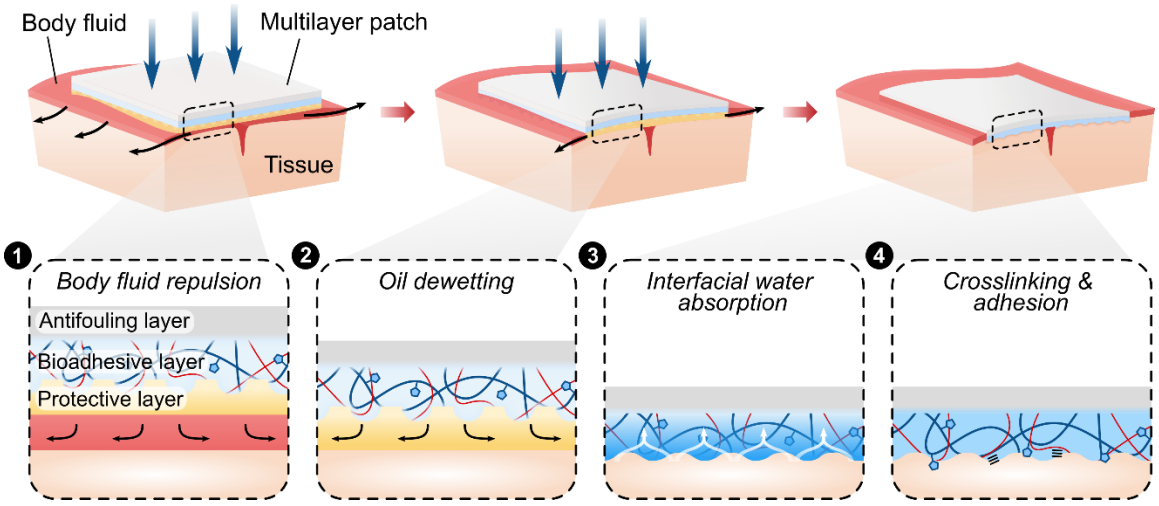

Figure 2-6: Schematic of the combined blood-repelling and adhesion mechanism of the multilayer patch. (1) As the patch is maneuvered toward the tissue, the infused silicone oil layer repels blood and prevents contamination of the bioadhesive layer. (2) External pressure application drives interfacial dewetting between the bioadhesive and the tissue substrate. (3) The bioadhesive layer makes contact with the tissue surface and undergoes rapid hydration, forming physical crosslinks. (4) Covalent bonds form between NHS ester functional groups in the bioadhesive network and primary amines on the tissue surface.

We can first consider the limiting case of a liquid positioned between two parallel molecularly smooth, hard surfaces [51]. When the surfaces approach one another under the influence of an external pressure perpendicular to the surfaces, the fluid is squeezed out horizontally. Viscous forces will pull the fluid toward the center of the contact region, and the pressure profile will follow a curve with a maximum at the central point. The dewetting of a single monolayer nucleates in the highest-pressure region of the contact interface (i.e., in the center of the contact region) and spreads toward the periphery. The hard solid walls, characterized by large

elastic moduli, prevent liquid rims from forming between monolayers, and dewetting occurs in a quantized process (monolayer by monolayer) until global dewetting is achieved [52]. The fluid squeeze-out time is thus determined by the viscosity of the fluid and the velocity with which the surfaces approach one another.

The situation becomes more complex when considering the elasticity of the tissue substrate, as well as the surface microstructure of the bioadhesive. In this scenario, local dewetting will nucleate at points where asperity contact occurs between the bioadhesive and tissue surfaces [53], [54]. Additionally, the relatively low elastic modulus of biological tissues (E ~ 1 MPa) renders it subject to elastic deformation, and can lead to the collection of liquid rims formed by expelled fluid surrounding a just-formed dry zone (**Figure 2-7**) [55]. Thus, it is possible for islands of interfacial fluids (e.g., residual blood and oil) to remain entrapped between dry zones at the interface, forming non-adhered regions in the contact area. Interfacial fluid entrapment occurs at the cost of actual contact area between the patch and the tissue, resulting in weakening of the adhesive bond. This effect motivates the need to experimentally determine the conditions with which maximal fluid squeeze-out can be achieved.

To consider the effect of tissue elasticity, we adopt the approach by Persson *et al.* and first evaluate a simplified system consisting of a thin liquid film contained between two flat surfaces: a soft material, e.g., the tissue substrate, and a rigid material, e.g., the bioadhesive material [52]. In the dry state, the PAA-NHS ester/chitosan material has an elastic modulus of 5.7 GPa and would be applied by means of a rigid surgical instrument, thus would not deform under hydrodynamic pressure. This approximation is appropriate for the fluid squeeze-out process (i.e., before the material becomes hydrated). For an interposed film of oil with initial thickness h, we can obtain

an expression for the energy required for nucleation of a dry patch, which corresponds to the creation of a contact bridge having a circular shape of radius R and thickness h (**Figure 2-7**).

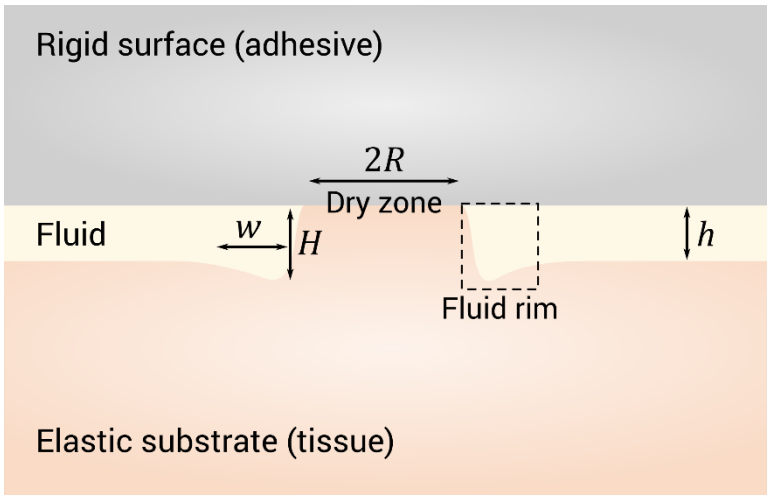

Figure 2-7: Schematic illustration of the nucleation of interfacial dewetting for a fluid between an elastic and a rigid substrate.

The elastic potential energy associated with the deformation of the tissue is $U_E = 1/2VE\varepsilon^2$, where E is the elastic modulus of the tissue, ε is the strain, and V is the volume over which the displacement extends. Here, the strain is of order $\varepsilon \sim h/R$ and $V \sim R^3$, so we can write $U_E \simeq 1/2Eh^2R$. The gain in surface energy is $U_A = \pi R^2\Delta\gamma + 2\pi Rh\gamma_{t/o}$, where $\Delta\gamma = \gamma_{t/ad} - (\gamma_{t/o} + \gamma_{o/ad})$ and $\gamma_{t/ad}$, $\gamma_{t/o}$, and $\gamma_{o/ad}$ are the tissue/adhesive, tissue/oil, and oil/adhesive interfacial energies. The total energy is therefore:

$$U_{total} = U_E + U_A \approx \frac{1}{2}Eh^2R + \pi R^2\Delta\gamma + 2\pi RH\gamma_{t/o} \qquad (2.6)$$

By taking $\partial U/\partial R = 0$ and neglecting the last term (that is, $2\pi RH\gamma_{t/o} \ll \pi R^2\Delta\gamma$), we can find the critical radius for nucleation, R_c:

$$R_c \simeq \frac{h^2}{4\pi\delta} \tag{2.7}$$

where $\delta = |\Delta\gamma|/E$ is characteristic length for nucleation [52]–[55]. When a contact bridge with $R > R_c$ is formed, a pressure gradient arising between the contact boundary and the rest of the system acts as a driving force for fluid squeeze-out. It has been experimentally found that nucleation typically occurs at lubrication film thicknesses much larger than e due to surface imperfections [37], [55].

Now consider the system under the influence of an external squeezing pressure [52]. When a dry patch of radius R is formed, the energy contribution arising from the applied pressure is:

$$U_p = -\int_0^R 2\pi r h P(r) dr + P(R)\pi R^2 h \tag{2.8}$$

Within the contact area, the pressure can be approximated as a Hertzian contact pressure between a rigid cylinder and an elastic half-space, which follows a parabolic profile:

$$P(r) = P_0\left[1 - \left(\frac{r}{R_0}\right)^2\right]^{1/2} \tag{2.9}$$

where P_0 is the maximum pressure, r is the distance from the center, and R_0 is the Hertz contact radius. Applying the chain rule to find $\frac{\partial U_p}{\partial t} = \left(\frac{\partial U_p}{\partial R}\right)\left(\frac{\partial R}{\partial t}\right)$, we get:

$$\frac{\partial U_p}{\partial t} = \left.\frac{\partial P(r)}{\partial r}\right|_{r=R} \pi R^2 h\dot{R} \tag{2.10}$$

From Eqn. (2.8), this becomes:

$$\frac{\partial U_p}{\partial t} = -\pi P_0 h R \dot{R} \left(\frac{R}{R_0}\right)^2 \left[1 - \left(\frac{R}{R_0}\right)^2\right]^{1/2} \tag{2.11}$$

Meanwhile, the rate of change of interfacial energy is:

$$\frac{\partial}{\partial t}(\Delta\gamma\pi R^2) = 2\Delta\gamma\pi R\dot{R} \tag{2.12}$$

And the rate of viscous dissipation in the fluid per unit volume is:

$$\Phi \sim \eta\dot{\gamma} \tag{2.14}$$

where $\dot{\gamma}$ is the shear strain rate. For an incompressible fluid, conservation of volume gives the following relation between the volume of the dry patch and the dimensions of the surrounding fluid rim:

$$\pi R^2 h \approx 2\pi R H w \tag{2.15}$$

Thus the viscous dissipation rate in the fluid rim is:

$$\Phi\Delta V \sim 2\pi R H w \eta \left(\frac{\dot{R}}{H}\right)^2 \tag{2.16}$$

If the gain in energy from the external pressure and change in interfacial energy is assumed to be dissipated entirely in the fluid rim, Eqns. (2.11), (2.12), and (2.15) yield:

$$\left\{2\Delta\gamma\pi R + \pi P_0 h R \left(\frac{R}{R_0}\right)^2 \left[1 - \left(\frac{R}{R_0}\right)^2\right]^{-1/2}\right\}\dot{R} \approx 2\pi R H w \eta \left(\frac{\dot{R}}{H}\right)^2 \tag{2.17}$$

Note that $\Delta\gamma < 0$ if the interfacial energies favor adhesion between the solid surfaces.

From conservation of volume (Eqn. 2.15), $Rh \approx 2Hw$, and assuming a quasistatic rim profile such that $H^2 \approx \delta w$, the following relation ensues:

$$\frac{w}{H} = \left(\frac{Rh}{2\delta^2}\right)^{1/3} \tag{2.18}$$

Then from (2.17), one can write using normalized variables :

$$\frac{t}{\tau} = \frac{4}{3}\int_0^{R/R_0} \frac{\tilde{r}^{1/3}}{1 + \alpha\tilde{r}^2(1-\tilde{r}^2)^{-1/2}}\, d\tilde{r} \tag{2.19}$$

where α is the dimensionless parameter

$$\alpha = \frac{P_0 h}{2|\Delta\gamma|} \tag{2.20}$$

Thus the external pressure acts as a driving force to accelerate dewetting as the fluid approaches the boundary of the contact area. Note also that the squeeze-out time τ has a dependency ~ $\left(\frac{\eta^3}{2\delta^2}\right)^{1/3}$ such that it increases with increasing fluid viscosity and elastic modulus, and decreases with increasing values of $|\Delta\gamma|$. In Figure 2-8, plots of R/R_0 vs. t/τ for various values of α show how increasing pressure (given a fixed $|\Delta\gamma|$) affects the growth profile of a dry zone. This is the result derived by Persson *et al.*, with a minor discrepancy in α (a factor of 3/2 vs. 1/2) owing to a different Hertzian pressure prefactor [52].

Eqns. (2.11) and (2.12) allow us to compare the relative importance of pressure and interfacial energy in driving fluid squeeze-out. Because $\left(\frac{R}{R_0}\right)^2\left[1-\left(\frac{R}{R_0}\right)^2\right]^{1/2}$ is mostly on the order of 1 from 0 to R_0, the ratio between the contributions of pressure and interfacial energy is on the order of:

$$P_0 : |\Delta\gamma|/h \tag{2.21}$$

For example, if $|\Delta\gamma|$ ~ 10 mN m^{-1} and h ~ 10^{-6} m, then for $P_0 \gg$ 10 kPa, the pressure force contribution dominates the squeeze-out dynamics.

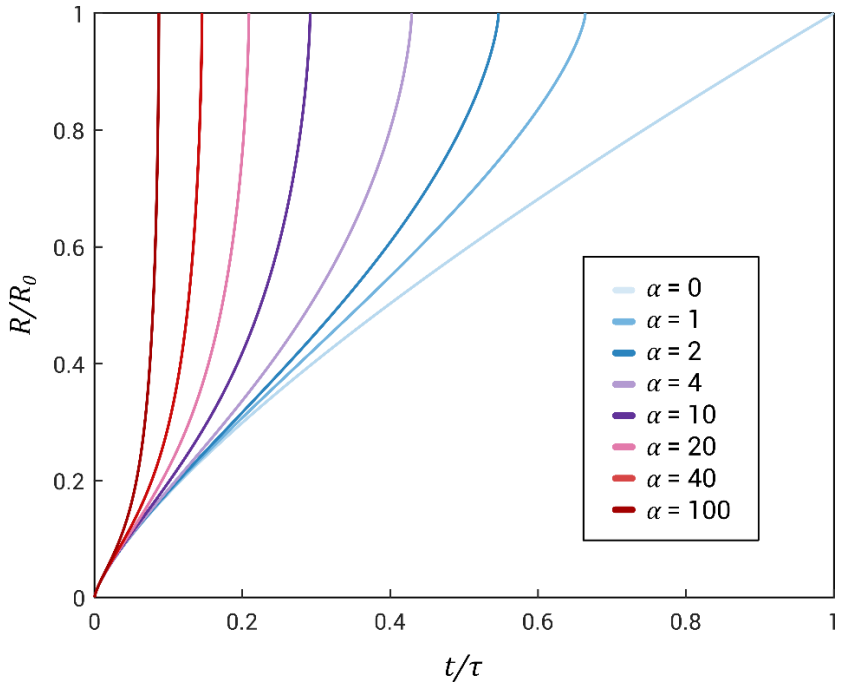

Figure 2-8: Normalized growth profiles of a dry zone evolving in the contact area between a rigid solid and an elastic substrate separated by a fluid film of thickness h for different values of α, where $\alpha = P_0h/2|\Delta\gamma|$. Higher values of α lead to acceleration of fluid squeeze-out.

Intuitively, one might expect that the effect of surface roughness would be to reduce contact area between the two solid surfaces and lead to a greater amount of interfacial fluid entrapment. To the contrary, experiments have found that rough-surface hydrogels can enhance the contact area with a glass substrate when squeezed together with a liquid layer interposed between them, compared to flat-surface hydrogels squeezed with glass under the same conditions [37]. This phenomenon can be reasoned by considering the role of surface roughness on the evacuation of interfacial fluid. When a flat surface is squeezed against an elastic substrate, the interposed fluid sustains the hydrodynamic pressure and a thin film remains until the surfaces are in very close proximity, i.e., near the critical length for nucleation relative to the characteristic length of surface asperities (as most real-life surfaces are not perfectly smooth). At this point, multiple dewetting domains form at once and islands of trapped fluid can occur due to contact boundary line instabilities and merging of boundary lines from separate nucleation points. When an island of trapped fluid is encircled by dry contact area, it effectively becomes "stuck" due to an insufficient pressure difference to drive squeeze-out [56]. On the other hand, for rough surfaces, the normal stress is primarily sustained by the apexes of the surface topography rather than by the interfacial fluid [37], [56]. As the applied pressure increases, interfacial fluid is free to drain through the channels between the apexes, and the contact area increases as the elastic substrate deforms. At longer timescales, hydration and swelling of the bioadhesive material will further increase the area of adhesion. A three-dimensional reconstruction of confocal micrographs taken at the interface of the microtextured bioadhesive (prepared using green fluorescent fluorescein-labeled chitosan) adhered to a soft gelatin hydrogel tissue phantom (prepared using red fluorescent Rhodamine Red™-labelled microbeads) shows the conformal adhesion interface between the microtextured bioadhesive surface and the gelatin hydrogel (**Figure 2-9**).

The presence of surface roughness also aids in the adhesion process by providing friction against the tissue, thus preventing the patch and the tissue from sliding against each other. Because flat films can sustain thin interfacial layers of fluid, the initial contact area is smaller than that in the rough case and the surfaces are more susceptible to sliding.

Control and reproducibility over contact behavior can best be obtained by controlling the pressure with which the patch is applied (e.g., by use of a surgical device fixed to deliver known loads). An upper bound for acceptable pressure applications to enable oil squeeze-out may be set by the limit at which tissue damage occurs for the particular surgical application. Details regarding the experimental procedure for determining an appropriate pressure threshold for the liquid-infused bioadhesive system are provided in Section 3.2.

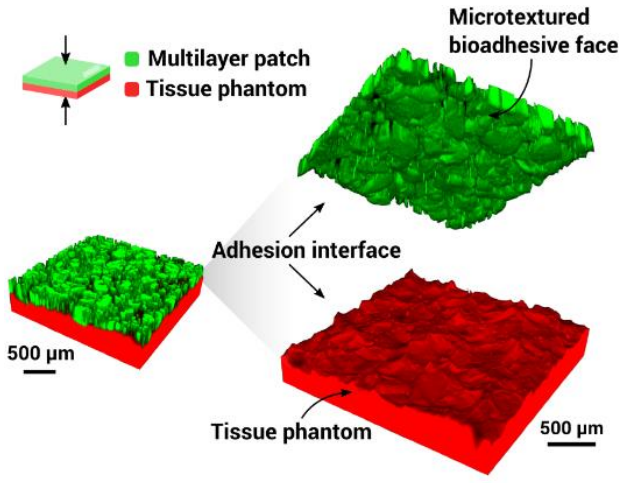

Figure 2-9: 3D reconstruction of confocal micrographs at the interface of adhesion between the microtextured bioadhesive face (green) and a gelatin-based tissue phantom (red).

2.4 DESIGN OF THE ANTIFOULING LAYER

The third component of the multilayer patch resides on the non-tissue-facing side which interacts with the surrounding physiological environment. This layer takes the form of a flexible and stretchable elastomer film interpenetrated with zwitterionic polymers. Its key function is to provide an antifouling surface to mitigate potentially harmful inflammatory responses and infectious complications.

2.4.1 PROPERTIES OF ZWITTERIONIC MATERIALS

Zwitterions describe unique molecules containing an equal number of separate positively- and negatively-charged functional groups. Naturally-occurring zwitterionic materials are abundant in biological systems (e.g., amino acids) and play distinct functional roles based on their charge group interactions. Synthetic zwitterionic materials were first reported in the 1950s [57]. Since then, zwitterionic materials have been used for a wide range of applications. Most notably, zwitterionic polymers have been found to exhibit remarkable antifouling properties due to their ability to attract a tight hydration shell while minimally disrupting the hydrogen-bonding structure of free water molecules [58]–[64]. Disturbance of this hydration shell carries a high energy cost which precludes the surface adsorption of bacteria and biomolecules (**Figure 2-10**). Owing to these features, zwitterionic polymers are attractive candidates for mitigating fouling by proteins, cells, and bacteria which are associated with clinical complications such as infection, blood coagulation, and postoperative adhesion formation.

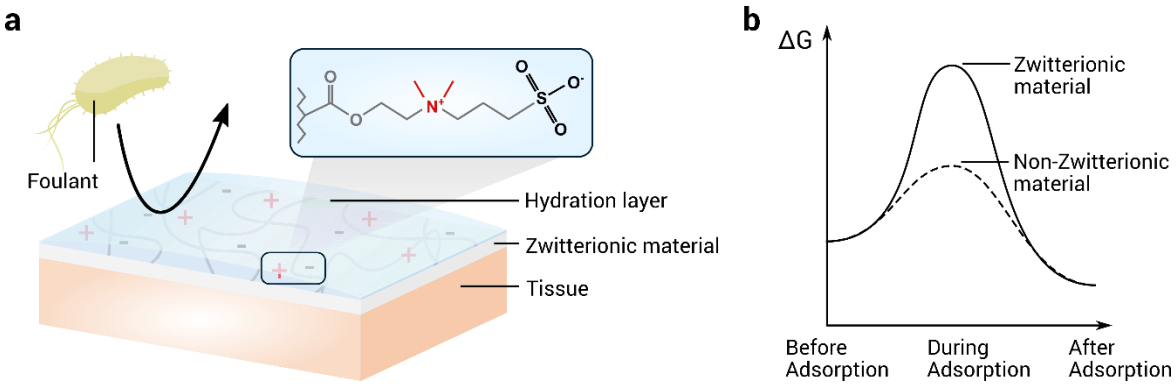

Figure 2-10: (a) Illustrated depiction of the hydration-based antifouling mechanism of a zwitterionic material containing sulfobetaine moieties. Foulant adsorption is prevented due to the formation of a tightly bound hydration layer caused by electrostatic interactions between water molecules and the charged ionic groups. (b) Qualitative reaction coordinate diagram showing the increased energy barrier for adsorption associated with displacing the hydration shell surrounding a zwitterionic material.

Two of the most commonly-used zwitterionic monomers contain cationic trimethyl ammonium groups and are classified as sulfobetaine (SB) and carboxybetaine (CB) based on their corresponding anions (sulfonate and carboxylate). Of these, SB monomers are more easily prepared and thus have a lower production cost, while CB monomers present greater design flexibility due to their amenability for functionalization of the -COOH groups [58]. Both moieties exhibit strong hydration behavior, which is a requisite for preventing protein adsorption. Despite their remarkable antifouling performance, poly(sulfobetaine) (pSB) and poly(carboxylbetaine) (pCB) based hydrogels typically suffer from poor mechanical properties, such as low toughness and stretchability, which hinders their long-term robustness and stability in physiological environments.

To solve this, several strategies have been reported to create zwitterionic betaine hydrogels with more favorable mechanical properties. These include combining the zwitterionic polymers with other polymers in interpenetrating networks, block copolymers, and nanocomposite hydrogels [65]–[69]. Here, we present a strategy for interpenetrating zwitterionic polymers into the surface of an elastomer film to achieve antifouling surface modification while maintaining the elasticity and mechanical strength of the bulk elastomer.

2.4.2 Surface-Interpenetration of Zwitterionic Polymers in an Elastomer Film

For the bulk material of the antifouling layer, thermoplastic polyurethane is an excellent candidate owing to its flexibility and strength, as well as its commercial availability. Medical-grade polyurethanes featuring a range of mechanical properties are widely manufactured for use in the preparation of different types of medical devices, including implants, artificial organs, and device coatings [70]. In the present work, a hydrophilic ether-based polyurethane which has undergone biocompatibility testing is used (purchased from AdvanSource Biomaterials). The polyurethane is soluble in 95% v/v ethanol, and the solution can be readily spin coated into a thin, flat film.

The zwitterionic surface-interpenetration process is depicted in Figure 2-11. First, the base film is created by spin-coating a solution containing polyurethane and a hydrophobic photoinitiator (e.g., benzophenone). After the film is fully dried, it is submerged into a aqueous solution containing the zwitterionic monomer (e.g., SB or CB monomers) and a hydrophilic photoinitiator (e.g., α-ketoglutaric acid). Due to the insolubility of the hydrophobic initiator in aqueous solution, it remains embedded in the polyurethane film and does not diffuse into the zwitterionic solution.

Polymerization of the zwitterionic solution occurs under the influence of UV irradiation, during which the hydrophobic initiators contained at the surface of the polyurethane film serve as grafting agents for the zwitterionic polymers to crosslink with the polyurethane chains [71]. In the reaction solution, the hydrophilic initiators assist in the polymerization of the zwitterionic monomers. After reaction, the film is thoroughly washed for several days to remove unreacted zwitterionic monomers and ungrafted polymers. The resultant film bears zwitterionic polymers interpenetrated at the surface, which can be experimentally validated using chemical analysis methods (e.g., Fourier-transform infrared spectroscopy (FTIR)) (see Section 3.3.1). The film can then be integrated with the bioadhesive layer by using a thin layer of spin-coated polyurethane to bond the two layers at the interface.

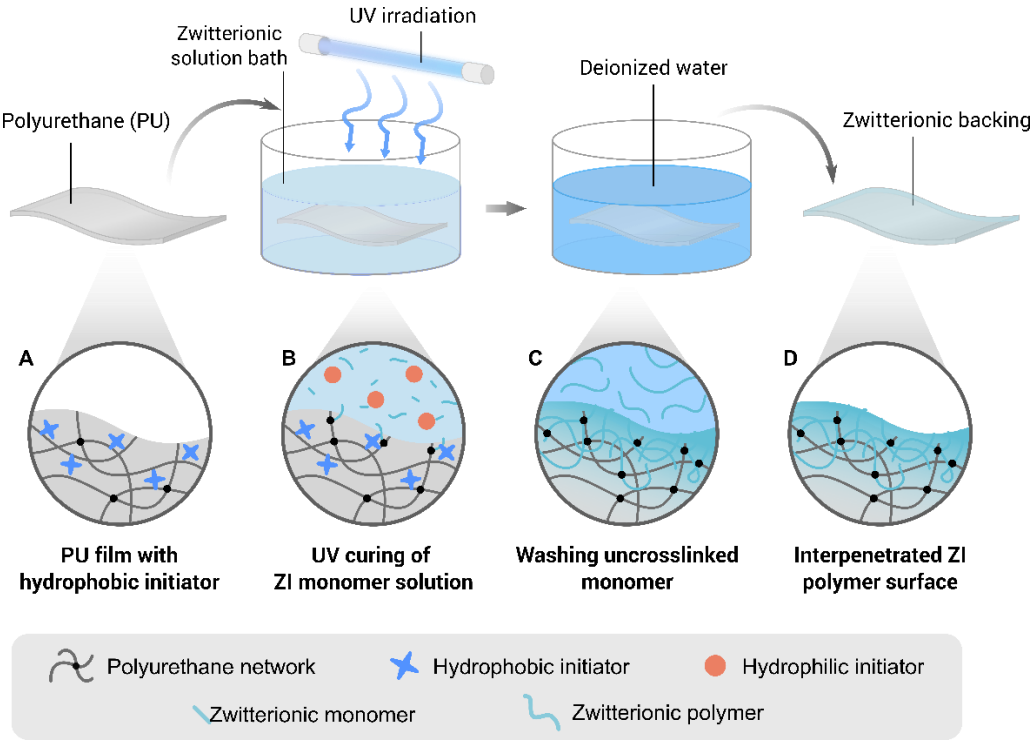

Figure 2-11: Illustrated schematic of the fabrication strategy for producing a zwitterionic polymer-interpenetrated polyurethane film. (a) A thin film of hydrophilic PU is treated with a hydrophobic initiator (i.e., benzophenone). (b) The treated PU film is submerged in a precursor solution containing the zwitterionic monomer and hydrophilic initiator, then cured in a UV chamber. (c) The sample is washed in a large volume of deionized water. (e) A zwitterionic-interpenetrated polyurethane film is retrieved.

CHAPTER 3

Characterization: Methods and Results

3.1 PREPARATION OF THE MULTILAYER PATCH

3.1.1 PREPARATION OF THE BIOADHESIVE LAYER

For the 30 w/w % acrylic acid, 2 w/w % chitosan (HMC+ Chitoscience Chitosan 95/500, 95 % deacetylation), 1 w/w % acrylic acid N-hydroxysuccinimide ester, 0.2 w/w % α-ketoglutaric acid, and 0.05 w/w % Poly(ethylene glycol dimethacrylate) (PEGDMA; Mn = 550) were dissolved in deionized water. For fluorescent microscopic visualization of the bioadhesive layer, fluorescein-labeled chitosan was used. The precursor solution was poured on a glass mold with spacers (the thickness is 210 μm unless otherwise mentioned) and cured in a UV chamber (284 nm, 10 W power) for 30 min. Right after curing, dry bioadhesive microparticles were sifted through a 100 μm sieve over the surface of the bioadhesive hydrogel. The resulting bioadhesive hydrogel with surface-embedded microparticles was then thoroughly dried and sealed in plastic bags with desiccant (silica gel packets) and stored at -20 °C prior to assembly with the non-adhesive layer.

3.1.2 PREPARATION OF THE BIOADHESIVE MICROPARTICLES

A bioadhesive film was first prepared by casting, curing, and drying the precursor solution described above. The fully dried bioadhesive material was then cryogenically grinded at 30 Hz

frequency for 2 min. The resulting bioadhesive microparticles were sealed in plastic bags with desiccant and stored at -20 °C until use.

3.1.3 Preparation of the Zwitterionic-Interpenetrated Elastomer

10 w/w % hydrophilic PU (HydroMedTM D3, Advansource Biomaterials) and 0.1 w/w % benzophenone dissolved in ethanol/water mixture (95:5 v/v) was spin-coated at 200 rpm. The spin-coated film was dried under airflow overnight, then submerged into an aqueous solution containing 35 w/w % [2-(Methacryloyloxy)ethyl]dimethyl-(3-sulfopropyl)ammonium hydroxide (DMAPS) and 5 w/w % α-ketoglutaric acid for 10 min, followed by curing in a UV chamber (284 nm, 10 W power) for 1 h. The resultant film was thoroughly washed in a large volume of deionized water for 3 days to remove unreacted reagents, then thoroughly dried under airflow.

3.1.4 Assembly of the Multilayer Patch

To combine the zwitterionic layer with the bioadhesive layer, a thin layer of 5 w/w % hydrophilic PU solution in ethanol/water mixture (95:5 v/v) was spin-coated at 400 rpm over the flat surface of the bioadhesive layer. The zwitterionic layer was then pressed on top and the entire assembly was thoroughly dried. The hydrophilic PU solution served as an adhesive between the zwitterionic layer and the bioadhesive layer by interpenetrating and drying between the two layers. To introduce the hydrophobic fluid layer, silicone oil (100 cSt viscosity) was first sterilized by filtration through a sterile membrane with 0.2 μm pore size to remove bacteria and other microorganisms. The sterilized silicone oil was then impinged on the microtextured surface of the bioadhesive layer.

3.2 ADHESION CHARACTERIZATION

3.2.1 BLOOD RESISTANCE

To evaluate the protective capacity of the silicone oil-infused bioadhesive surface, samples of the patch with and without silicone oil were submerged in blood and their fouling behaviors were compared (**Figure 3-1a**). When submerged in a porcine blood bath, the patch without the silicone oil layer is immediately wetted by the blood and loses its adhesive capability, whereas the patch with the protective silicone oil layer resists blood contamination and remains intact. To further investigate the effect of the surface microtopography on the stability of the fluid layer, patches with flat and microtextured bioadhesive surfaces were subjected to vigorous shaking in a porcine blood bath. While the multilayer patch with a flat bioadhesive surface shows substantial blood contamination after shaking, the patch comprising a microtextured surface exhibits robust protection of the bioadhesive layer against vigorous blood flow, supporting the significance of the microtextured design of the bioadhesive layer in order to achieve stable contaminant-repellent properties (**Figure 3-1b**).

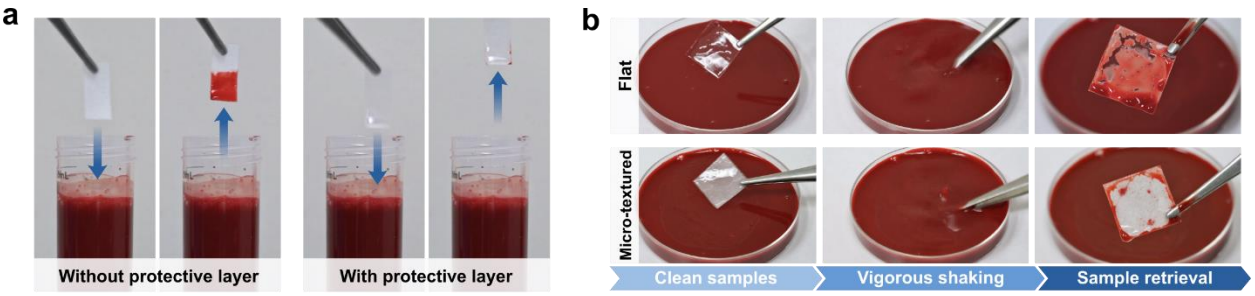

Figure 3-1: (a) Photographs of multilayer patches with and without the hydrophobic fluid layer before and after submerging in a porcine blood. (b) Photographs of the multilayer patches with flat and microtextured bioadhesive layers before and after vigorously shaking in a porcine blood bath.

3.2.2 INTERFACIAL FLUID ENTRAPMENT

To determine the optimal pressure conditions for removing interfacial blood and maximizing the contact area of adhesion, the amount of residual blood entrapped between patches and gelatin hydrogel tissue phantoms was quantified following adhesion under varying applied pressures covered with porcine blood (**Figures 3-2** and **3-3**). The gelatin hydrogel tissue phantoms were prepared by dissolving 10 w/w % gelatin (300 bloom) in deionized water at 40 ℃, pouring the solution into a glass mold with 5 mm spacers, and then cooled at room temperature for 1 h. A sample of the multilayer patch (25.4 mm in width and 25.4 mm in length) was coated with silicone oil (100 cSt viscosity), then placed onto a gelatin hydrogel tissue phantom submerged in blood with the hydrophobic oil layer facing downward. The multilayer patch was pressed against the tissue phantom at varying applied pressures using a mechanical testing machine (2.5 kN load-cell, Zwick/Roell Z2.5) for 5 s. The blood entrapped at the adhered patch-tissue phantom interface was visualized by taking photographs. To quantify the blood-entrapped area, the photographs were processed and analyzed by using ImageJ (**Figure 3-3**).

The adhesive shear strength of patches adhered to blood-covered porcine skin tissues under the same varying pressures was also measured (**Figure 3-2c** and **3-4**). As the applied pressure increases, the area of entrapped blood decreases while the adhesive shear strength increases. When the applied pressure exceeds 77.5 kPa, the amount of entrapped blood and the adhesive shear strength both reach plateau values, indicating that a threshold pressure of 77.5 kPa can effectively repel most of the interfacial blood and activate optimal adhesion of the multilayer patch. Notably, this level of pressure (i.e., around 100 kPa) can be readily applied by surgical end effectors such as staplers and balloons.

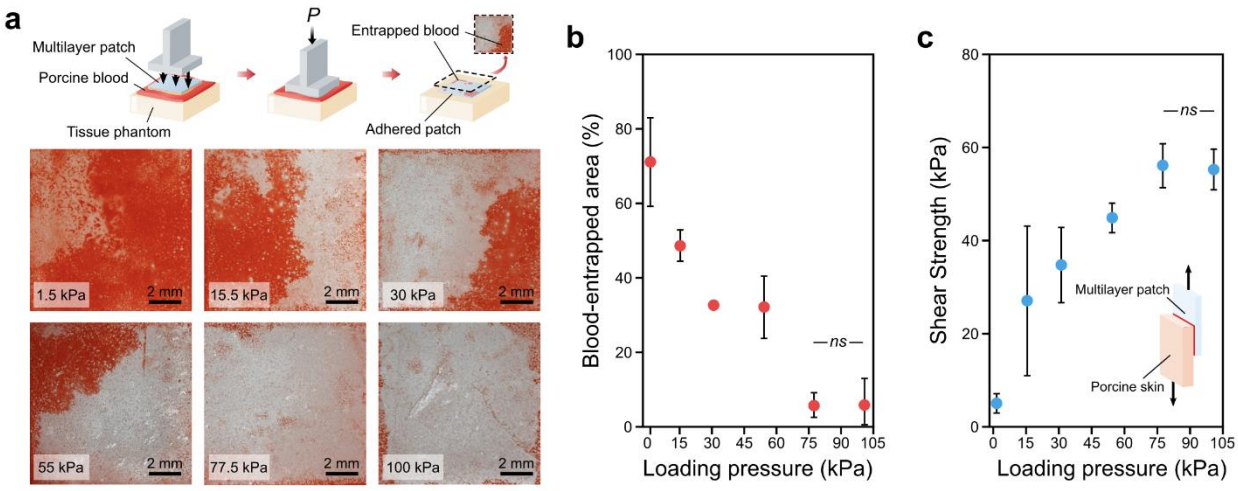

Figure 3-2: Characterization of blood repellence and adhesion performances of the multilayer patch under varying applied pressures. (a) Representative photographs of the interfaces between the adhered multilayer patches and tissue phantom gelatin hydrogels. (b) Percentage of blood-entrapped area at the interface as a function of applied pressure. c) Shear strength of adhered multilayer patches and blood-covered porcine skin as a function of applied pressure. Values in (b,c) represent the mean and the standard deviation (n = 2). P values are determined by a Student's t-test; * $p \leq 0.05$; ** $p \leq 0.01$; *** $p \leq 0.001$.

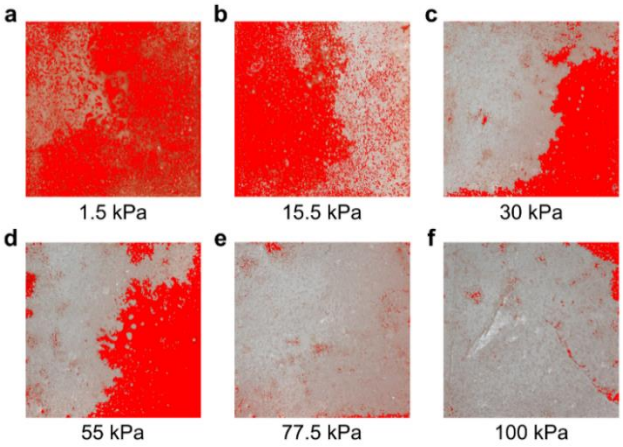

Figure 3-3: Representative processed images for the quantification of blood entrapment at the area of adhesion between the patches and blood-covered gelatin hydrogel tissue phantom compressed at (a) 1.5 kPa, (b) 15.5 kPa, (c) 30 kPa, (d) 55 kPa, (e) 77.5 kPa, and (f) 100 kPa for 5 s. Photographs were processed by globally thresholding in ImageJ, then analyzed to quantify the percentage of blood-entrapped area.

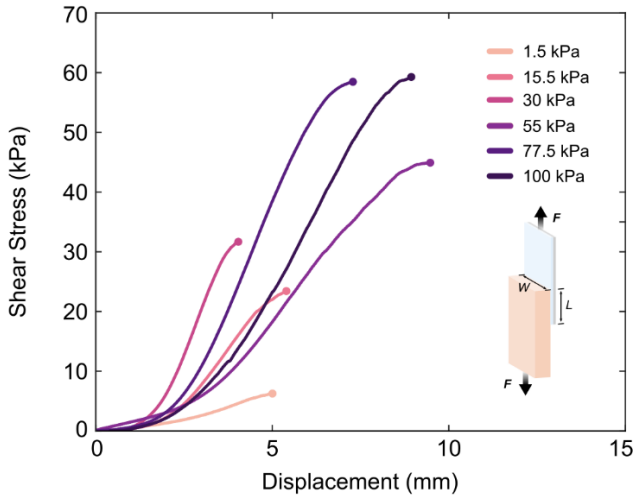

Figure 3-4: Shear stress vs. displacement curves for lap-shear tests of multilayer patches adhered to blood-covered porcine skins with varying applied pressures (1.5, 15.5, 30, 55, 77.5, and 100 kPa) for 5 s.

3.2.3 ADHESION STRENGTH

To quantitatively evaluate the ability of the multilayer patch to form adhesion in blood, samples of the patch were adhered with porcine skin tissues submerged in a blood bath using an applied pressure of 77.5 kPa, and quantitatively assessed by 180-degree peel tests (ASTM F2256), lap-shear tests (ASTM F2255), and tensile tests (ASTM F2258) to measure the interfacial toughness, shear strength, and tensile strength of the adhered samples, respectively (**Figures 3-5** and **3-6**).

To measure interfacial toughness, the adhered samples with widths of 2.5 cm were prepared and tested by the standard 180-degree peel test (ASTM F2256) using a mechanical testing machine (2.5-kN load-cell, Zwick/Roell Z2.5). All tests were conducted with a constant peeling speed of 50 mm min^{-1}. The measured force reached a plateau as the peeling process entered the steady-state. Interfacial toughness was determined by dividing two times of the plateau force (for 180-degree peel test) with the width of the tissue sample (**Figure 3-6a**). Hydrophilic nylon filters (1 μm pore size, TISCH Scientific) were applied as a stiff backing for the multilayer patch. Poly(methyl methacrylate) (PMMA) films (with a thickness of 50 μm; Goodfellow) were applied using cyanoacrylate glue (Krazy Glue) as a stiff backing for the tissues.

To measure shear strength, the adhered samples with an adhesion area of 2.5 cm in width and 1 cm in length were prepared and tested by the standard lap-shear test (ASTM F2255) with a mechanical testing machine (2.5-kN load-cell, Zwick/Roell Z2.5). All tests were conducted with a constant tensile speed of 50 mm min^{-1}. Shear strength was determined by dividing the maximum force by the adhesion area (**Figure 3-6b**). Hydrophilic nylon filters were applied as a stiff backing for the multilayer patch. PMMA films were applied using cyanoacrylate glue (Krazy Glue) as a stiff backing for the tissues.

To measure tensile strength, the adhered samples with adhesion area of 2.5 cm in width and 2.5 cm in length were prepared and tested by the standard tensile test (ASTM F2258) with the mechanical testing machine. All tests were conducted with a constant tensile speed of 50 mm min^{-1}. Tensile strength was determined by dividing the maximum force with the adhesion area (**Figure 3-6c**). Aluminum fixtures were applied by using a cyanoacrylate glue to provide grips for the tensile tests.

The interfacial toughness, shear strength, and tensile strength of porcine skin tissues adhered using various commercially-available tissue adhesives were measured as well, including fibrin-based Tisseel, albumin-based Bioglue, polyethylene glycol (PEG)-based Coseal, and cyanoacrylate-based Histoacryl (**Figure 3-7**). Compared to these commercially-available tissue adhesives, the multilayer patch resists blood contamination and achieves significantly higher interfacial toughness (536.7 ± 93.4 J m-2), shear strength (56.1 ± 4.7 kPa), and tensile strength (65.0 ± 8.0 kPa).

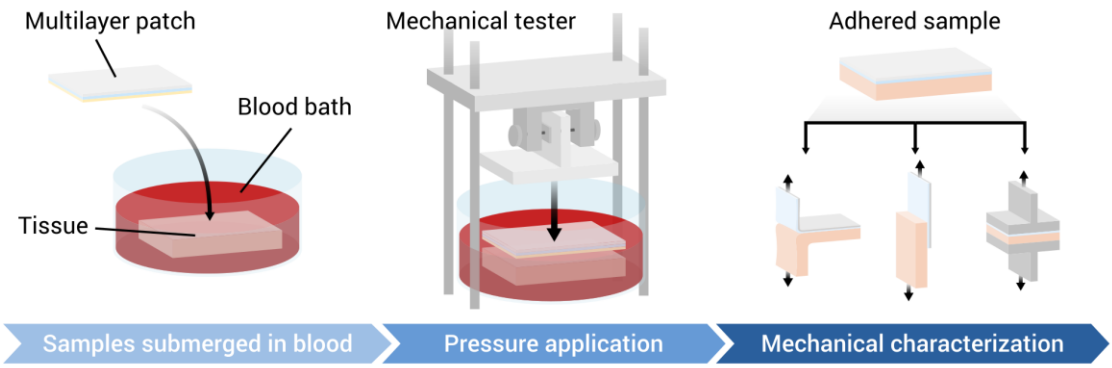

Figure 3-5: Experimental setup for the adhesion characterization of the multilayer patch and tissues submerged in blood. First, a sample of porcine tissue is covered with heparinized porcine blood. The multilayer patch is placed in the blood bath, then a mechanical tester applies a controlled pressure to adhere the patch to the tissue. After 5 s of pressure application, the adhered sample is collected for mechanical characterization to measure interfacial toughness, shear strength, or tensile strength, following ASTM standards F2256, F2255, and F2258.

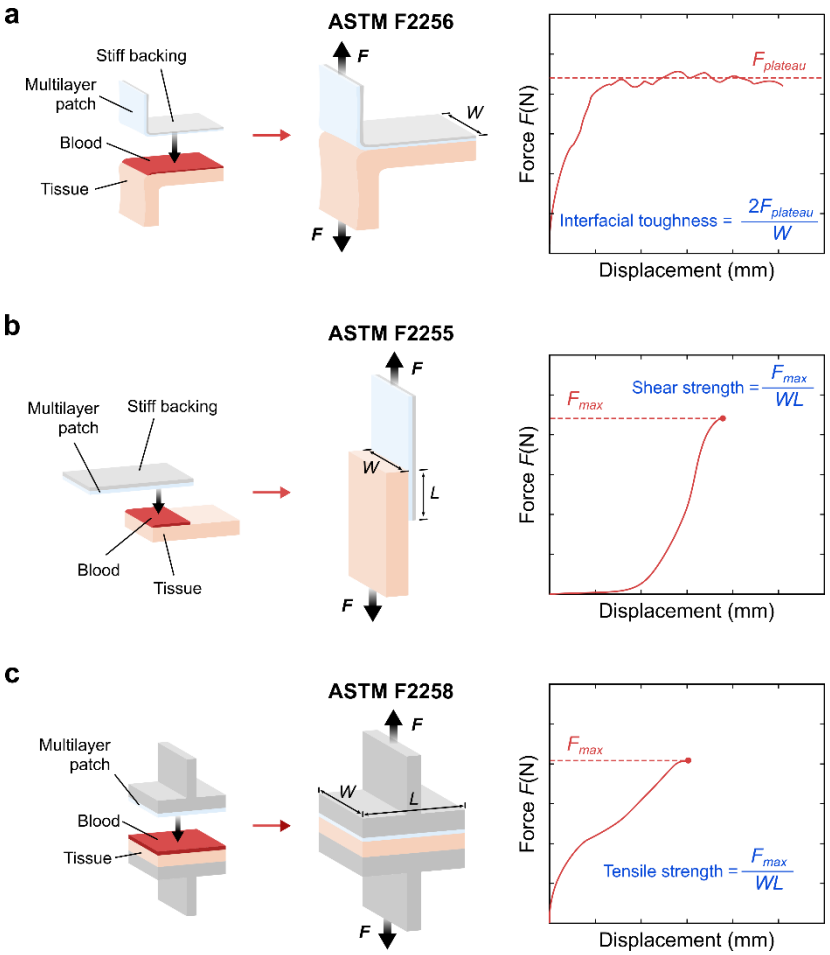

Figure 3-6: Schematic illustrations of the experimental setup for (a) interfacial toughness measurements based on the standard 180-degree peel test (ASTM F2256); (b) shear strength measurements based on the standard lap-shear test (ASTM F2255); and (c) tensile strength measurements based on the standard tensile test (ASTM F2258).

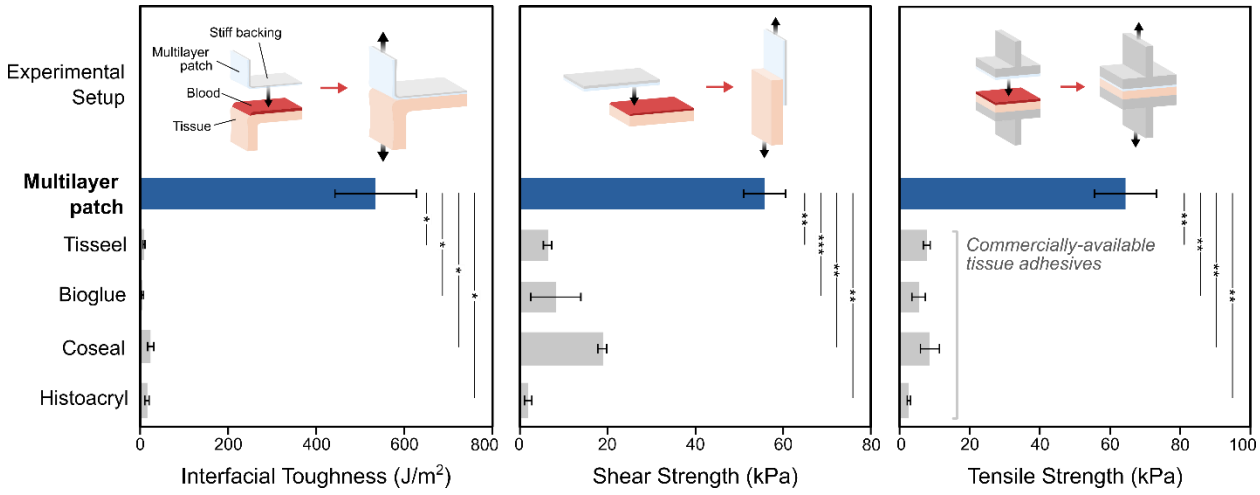

Figure 3-7: Comparison of adhesion performances of the multilayer patch and various commercially-available tissue adhesives, adhered to porcine skin coated with porcine blood. Values represent the mean and the standard deviation (n = 3). *P* values are determined by a Student's *t*-test; ns, not significant ($p > 0.05$); * $p \leq 0.05$; ** $p \leq 0.01$; *** $p \leq 0.001$.

3.3 MECHANICAL PROPERTIES

3.3.1 MECHANICAL PROPERTIES OF THE PATCH

The tensile properties and fracture toughness of the samples were measured using pure-shear tensile tests of thin rectangular samples (10 mm in length, 30 mm in width, and 0.5 mm in thickness) with a mechanical testing machine (20-N load-cell, Zwick/Roell Z2.5). All tests were conducted with a constant tensile speed of 50 mm min^{-1}. The fracture toughness of the samples was calculated based on tensile tests of unnotched and notched samples (**Figure 3-8**). The measured shear modulus of the fully assembled multilayer patch is 70 kPa, and the measured fracture toughness of the multilayer patch is 2,100 J m^{-2}.

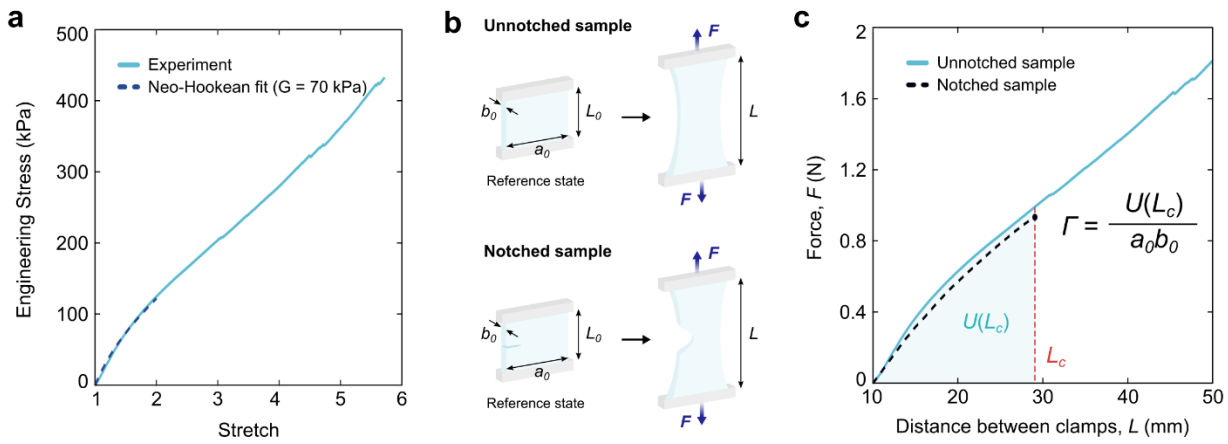

Figure 3-8: Mechanical characterization of the multilayer patch. (a) Engineering stress vs. stretch curve of the multilayer patch. The measured shear modulus of the multilayer patch is 70 kPa. (b) Schematic illustrations of a pure-shear test for unnotched and notched samples. (c) Force vs. distance between clamps curves for the unnotched and notched antifouling face. L_c indicates the critical distance between the clamps at which the notch turns into a running crack. The measured fracture toughness of the multilayer patch is 2,100 J m^{-2}.

3.3.2 MECHANICAL PROPERTIES OF THE ANTIFOULING LAYER

The fracture toughness of the zwitterionic-interpenetrated polyurethane layer was compared with a pure zwitterionic hydrogel (**Figures 3-9** and **3-10**). To prepare the zwitterionic hydrogel, 50 w/w % DMAPS, 0.5% w/w % Irgacure 2959, and 0.5% w/w % PEGDMA were dissolved in deionized water. The precursor solution was then poured on a glass mold with 1 mm spacers and cured in a UV chamber (284 nm, 10 W power) for 60 min. Compared to the zwitterionic hydrogel (fracture toughness 0.35 J m^{-2} and stretchability less than 1.5 times of the original length), the zwitterionic-PU layer exhibits superior mechanical properties (fracture toughness around 420 J m^{-2} and stretchability over 3.5 times of the original length).

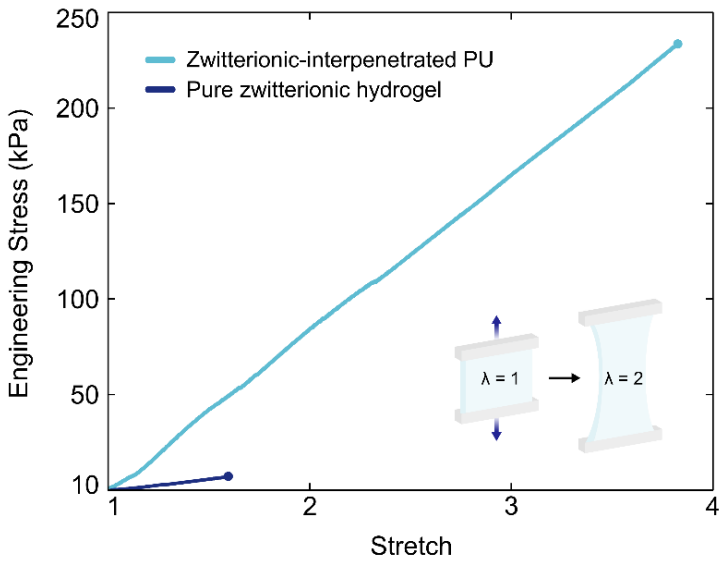

Figure 3-9: Representative engineering stress vs. stretch curves for the zwitterionic-interpenetrated polyurethane layer and a pure zwitterionic hydrogel.

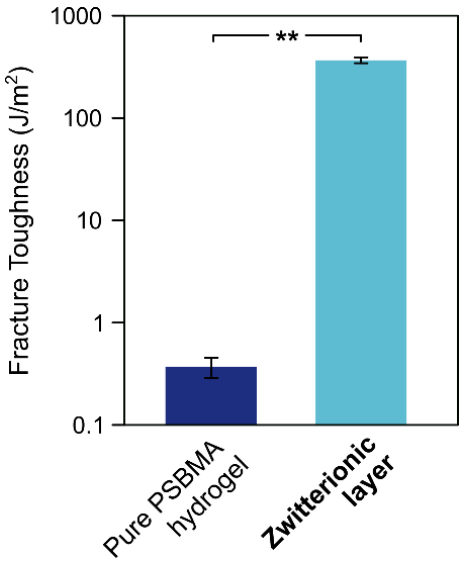

Figure 3-10: Fracture toughness of a pure zwitterionic hydrogel (0.35 J m^{-2}) and the zwitterionic-interpenetrated elastomer layer (420 J m^{-2}).

3.4 ANTIFOULING PERFORMANCE

3.4.1 CHEMICAL CHARACTERIZATION

To verify the presence of polysulfobetaines in the zwitterionic-interpenetrated polyurethane film, the surface was characterized by a transmission Fourier transform infrared spectroscope (FTIR 6700, Thermo Fisher) using a Germanium attenuated total reflectance (ATR) crystal (55 deg) (**Figure 3-11**). Compared to pristine PU, the FTIR spectrum for the zwitterionic-interpenetrated PU shows strong absorbance peaks at 1020 cm^{-1} and 1180 cm^{-1}, which correspond to vibrations of the sulfonate group ($-SO_3$) present in the sulfobetaine moiety [61].

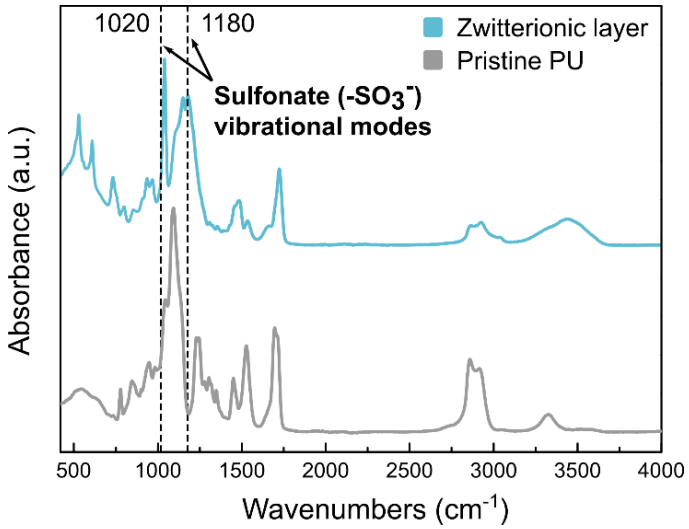

Figure 3-11: FTIR spectra of the zwitterionic layer and unmodified pristine hydrophilic PU; peaks at 1020 cm^{-1} and 1180 cm^{-1} correspond to vibrational modes of the sulfonate group ($-SO3^-$).

3.4.2 Bacterial Adhesion

To characterize the antifouling performance of the zwitterionic layer, its capability to mitigate *in vitro* bacterial adhesion was evaluated (**Figure 3-12**). Bacterial attachment to implanted materials can lead to biofilm formation and surgical site infection, which cause significant patient morbidity and substantial healthcare costs due to the need for additional procedures and antimicrobial therapies. To evaluate the antimicrobial performance of the zwitterionic layer, various patches with non-adhesive faces comprised of a hydrophobic polymer (polydimethylsiloxane, PDMS), a hydrophilic polymer (pristine hydrophilic PU), and the zwitterionic-interpenetrated elastomer were incubated with a green-fluorescent protein (GFP)-expressing *Escherichia coli* (*E. coli*).

An engineered *Escherichia coli* (*E. coli*) strain that constitutively expresses green fluorescent protein (GFP) was prepared by following a previously reported protocol and cultured

in Luria-Bertani broth (LB broth) overnight at 37 °C. 1 µL of bacteria culture diluted in 1 mL of fresh LB broth was placed on samples (1 cm × 1 cm) and incubated for 24 h at 37 °C [71]. After incubation, the samples were taken out and rinsed with phosphate buffered saline (PBS) to remove the free-floating bacteria, and imaged with a fluorescence microscope (Eclipse LV100ND, Nikon). The number of adhered *E. coli* on the samples per unit area (mm^2) were counted by ImageJ. In contrast to the patches featuring hydrophobic (~ 1,370 counts mm^{-2}) and hydrophilic non-adhesive layers (~ 1,360 counts mm^{-2}), the patch with the zwitterionic layer exhibits a significantly lower level of *E. coli* adhesion (~ 0.9 counts mm^{-2}).

3.4.3 THROMBOGENICITY

The antifouling performance of the zwitterionic layer was further assessed by evaluating its capacity to resist the adsorption of fibrinogen in porcine whole blood. Surface attachment of fibrinogen leads to the formation of a fibrin meshwork, which serves as the basis of a blood clot. Thus, the surface coverage of fibrin can indicate the potential for a biomaterial to induce platelet accumulation, activation, and thrombus formation, which are undesirable for applications in which the bioadhesive interfaces with a bloodstream. Samples with non-adhesive layers comprised of a hydrophobic polymer (PDMS), a hydrophilic polymer (pristine hydrophilic PU), and the zwitterionic-interpenetrated elastomer were submerged in a blood bath containing heparinized porcine whole blood spiked with Alexa Fluor 488-tagged fibrinogen [72].

A 5 v/v % solution of fetal bovine serum (FBS) in PBS used to block the wells of a 24-well plate for 30 min. The wells were rinsed with PBS, then 6 mm-diameter samples were placed in the blocked wells. The samples were submerged in porcine blood spiked with Alexa Fluor® 488-labeled human fibrinogen conjugate (66 µg fibrinogen mL^{-1} blood, Thermo Fisher) and incubated

on a shaker in 220 rpm at room temperature for 60 min. The samples were gently rinsed in PBS and fixed for 1 hour in 2.5 v/v% glutaraldehyde in 0.1 M phosphate buffer. The samples were then imaged with a fluorescence microscope (Eclipse LV100ND, Nikon) and analyzed by using ImageJ.

Exhibiting similar behavior to the results for bacterial adhesion, the patch with the zwitterionic layer shows significantly lower levels of fibrin deposition (~0.1% areal coverage) compared to the patches with hydrophobic (~3.09% areal coverage) and hydrophilic faces (~2.16% areal coverage) (**Figure 3-13**). These results suggest a lower thrombogenic risk associated with the zwitterionic material in contact with whole blood.

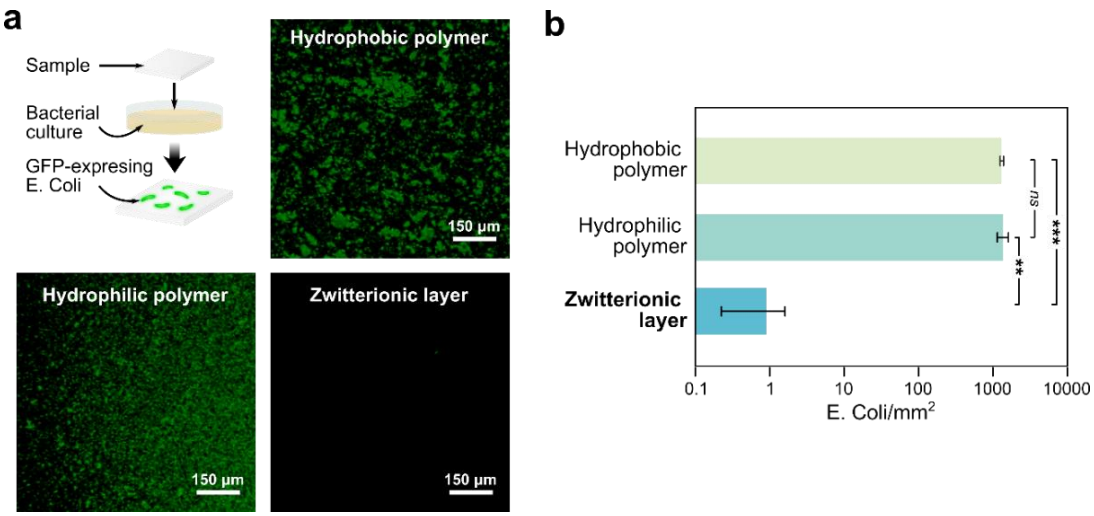

Figure 3-12: (a) Representative fluorescent micrographs of GFP-expressing *E. Coli* adhered to a hydrophobic polymer (PDMS), a hydrophilic polymer (PU), and the zwitterionic layer following 24 h incubation. (b) The number of adhered *E. Coli* per mm^2 for each substrate.

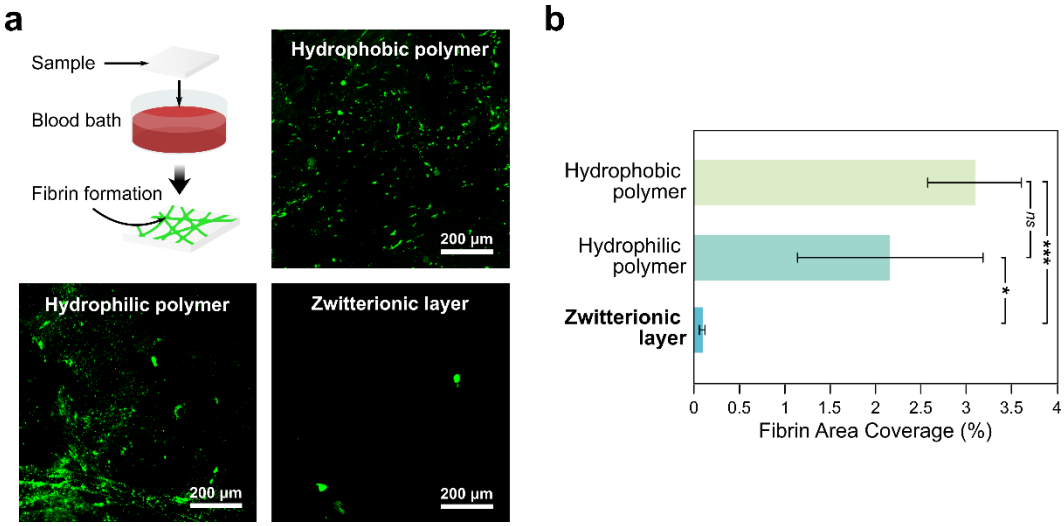

Figure 3-13: (a) Representative fluorescent micrographs of fibrin network formation on a hydrophobic polymer (PDMS), a hydrophilic polymer (PU), and the zwitterionic layer after 60 min of exposure to porcine whole blood spiked with fluorescently-tagged fibrinogen. (b) Fibrin area coverage (%) for each substrate.

3.5 BIOCOMPATIBILITY AND BIODEGRADATION

3.5.2 *IN VIVO* IMPLANTATION: SMALL ANIMAL MODEL

All animal surgeries were reviewed and approved by the Committee on Animal Care at the Massachusetts Institute of Technology. Female Sprague Dawley rats (225-250 g, Charles River Laboratories) were used for all *in vivo* studies. Before implantation, the multilayer patch was prepared using aseptic techniques and was further sterilized for 3 hours under UV light. For implantation in the dorsal subcutaneous space, rats were anesthetized using isoflurane (1–2% isoflurane in oxygen) in an anesthetizing chamber. Anesthesia was maintained using a nose cone. The back hair was removed and the animals were placed over a heating pad for the duration of the surgery. The subcutaneous space was accessed by a 1-2 cm skin incision per implant in the center of the animal's back. To create space for implant placement, blunt dissection was performed from the incision towards the animal shoulder blades. multilayer patches with hydrophobic polymer (PDMS) faces ($n = 4$), hydrophilic polymer (pristine hydrophilic PU) faces ($n = 4$), and zwitterionic faces ($n = 4$) with the size of 10 mm in width and 20 mm in length were placed in the subcutaneous pocket created above the incision without detachment. The incision was closed using interrupted sutures (4-0 Vicryl, Ethicon) and 3-6 ml of saline were injected subcutaneously. Up to four implants were placed per animal ensuring no overlap between each subcutaneous pocket created. After 2 or 4 weeks following the implantation, the animals were euthanized by CO_2 inhalation. Subcutaneous regions of interest were excised and fixed in 10% formalin for 24 hours for histological analysis.

3.5.2 *IN VIVO* FIBROUS ENCAPSULATION

To evaluate the biocompatibility and *in vivo* antifouling performance of the multilayer patch, the fibrous capsule formed in response to a variety of patches was measured and compared. As described in the preceding section, rats were implanted with patches containing non-adhesive layers comprised of a hydrophobic polymer (PDMS), a hydrophilic polymer (pristine hydrophilic PU), and the zwitterionic-interpenetrated elastomer. At time points of 2 and 4 weeks following implantation, the tissues were collected and fixed and submitted for histological processing and Masson's Trichrome staining. The thickness of fibrous capsule was measured under a bright-field digital microscope (Eclipse LV100ND, Nikon) based on histology slides of each sample.

The formation of a thick fibrotic encapsulation around the surgical site is highly undesirable and can result in complications such as organ stricture and postoperative adhesions [7], [29]. After 2 weeks of implantation, histological analysis shows that the patch containing the zwitterionic layer exhibits a significantly thinner fibrous capsule around the patch (145 ± 29 μm) compared to the patches with hydrophobic (574 ± 125 μm) and hydrophilic polymer layers (185 ± 16 μm) (**Figure 3-14a**). After 4 weeks of implantation, the patch with the zwitterionic layer maintains a similar thickness of fibrous capsule around the patch (135 ± 7 μm) to the 2-week results, whereas the patches with hydrophobic (1163 ± 138 μm) and hydrophilic (307 ± 73 μm) polymer layers exhibit significantly thicker fibrous capsules than their respective 2-week results (**Figure 3-14b**). In summary, these results suggest that the zwitterionic layer of the multilayer patch possesses favorable capacities to resist excessive fibrosis around the injury site.

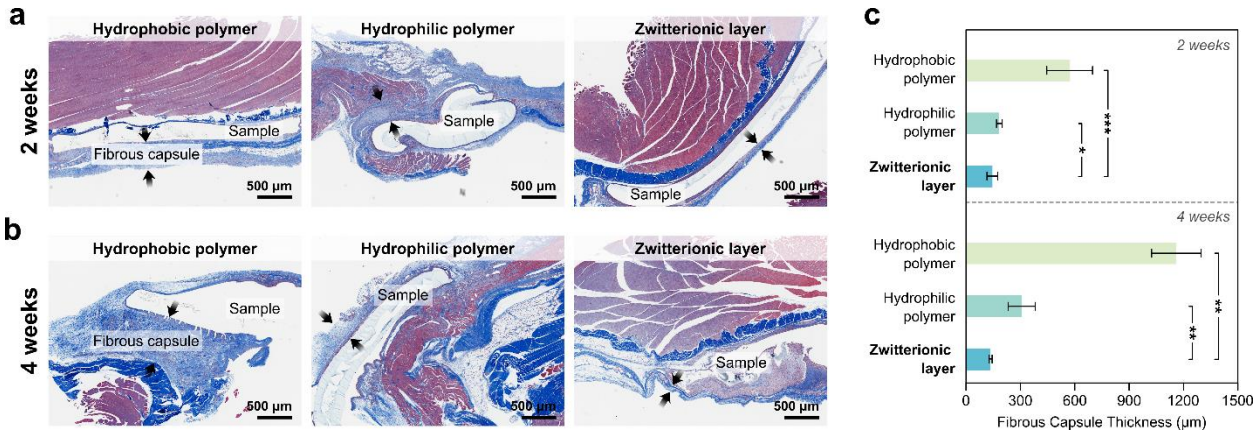

Figure 3-14: (a,b) Representative histological images stained with Masson's trichrome for *in vivo* rat dorsal subcutaneous implantation of patches with non-adhesive faces comprised of a hydrophobic polymer (PDMS, left), a hydrophilic polymer (PU, middle), and the zwitterionic layer (right) after 2 weeks (a) and 4 weeks (b). (c) Fibrous capsule thickness formed around the implanted samples after *in vivo* the implantation. Values in (c) represent the mean and the standard deviation ($n = 4$). *P* values are determined by a Student's *t*-test; * $p \leq 0.05$; ** $p \leq 0.01$; *** $p \leq 0.001$.

3.5.3 Inflammation Scoring

To further investigate the *in vivo* biocompatibility of the multilayer patch, histological images of the implanted samples were submitted for histological analysis and evaluated by a blinded pathologist (**Figure 3-15**). The degree of inflammation at the implantation site for the zwitterionic layer-containing patch received average scores of 1.33 and 1.67 after 2 and 4 weeks, respectively, which fall within the "very mild" to "mild" inflammation range. These results indicate that the multilayer patch elicits low levels of acute and chronic inflammation.

3.5.4 BIOSTABILITY

The multilayer patch exhibits stability for several weeks at the implantation site *in vivo* (**Figure 3-16**). Because the bioadhesive layer is comprised of PAA-NHS ester crosslinked with biodegradable linkages and the biopolymer chitosan, it can be left to undergo enzymatic biodegradation within the body if it is intended to be implanted without recurrent surgery. The degradation rate can be tuned by changing the type of biopolymer used in the bioadhesive material (e.g., gelatin or alginate instead of chitosan) or the ratio of crosslinking agent used.

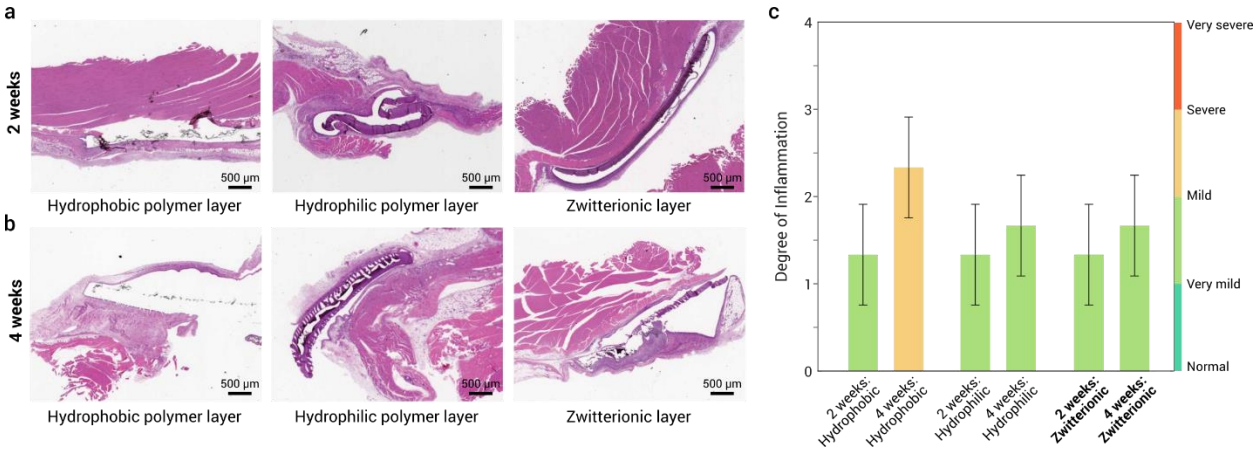

Figure 3-15: *In vivo* inflammation scoring of the multilayer patch. Representative H&E histological images of multilayer patches with non-adhesive layers comprised of a hydrophobic polymer, a hydrophilic polymer, and a zwitterionic-interpenetrated elastomer layer implanted into the dorsal subcutaneous spaces of rats after a) 2 weeks and b) 4 weeks. c) Histological evaluation of the degree of inflammation at the implantation sites by a blinded pathologist. Degree of inflammation is scored wherein 0 = normal, 1 very mild, 2 = mild, 3 = severe, and 4 = very severe. Values represent the mean and standard deviation (n = 3).

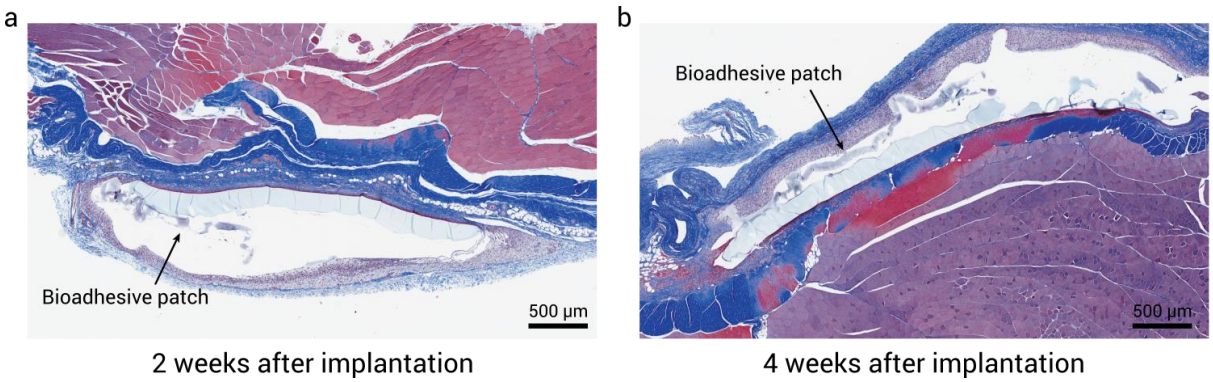

Figure 3-16: *In vivo* stability of the multilayer patch. Representative histological images stained with Masson's trichrome of samples implanted into the dorsal subcutaneous spaces of rats for a) 2 weeks and b) 4 weeks. At 4 weeks after implantation, the bioadhesive patch begins to exhibit visual signs of gradual degradation and decomposition.

CHAPTER 4

Minimally Invasive Surgical Applications

4.1 ORIGAMI-INSPIRED DESIGN

In order for the patch to achieve utility in minimally invasive surgery, it must be amenable to navigation through narrow spaces and facile deployment on demand. With this in mind, inspiration was drawn from origami: the Japanese art of paper folding. Due to the solid tape-like form-factor of the multilayer patch, it can be folded into compact, 3-dimensional shapes that are programmed to expand upon actuation of surgical end effectors. This section discusses the material properties that enable this strategy to be adapted, and describes the prototypical designs developed for several *ex vivo* proof-of-concept demonstrations.

4.1.1 PLASTIC TO RUBBERY STATE TRANSITION

The basis of the origami-inspired design strategy lies in the transition of the bioadhesive polymer network from the glassy state, during which it can maintain a deformed shape, to the rubbery state, during which the strain at its folded hinges is released. The general strategy is alike that of shape memory polymers (SMPs), which are pre-deformed into temporal shapes in the glassy phase with the intent of recovering their original shapes in response to an external stimulus, such as temperature. Here, the dry bioadhesive material is in the glassy state at room temperature. When the patch is folded, the elastomer is constrained by the bioadhesive material due to its higher

rigidity, such that the creases are held in place. Hydration of the bioadhesive material is the driving stimulus for the phase transition, which occurs upon tissue contact when interfacial water is absorbed. Hydration works by lowering the glass transition temperature of the material. As a result, the patch returns to the soft rubbery state and conforms to the tissue surface (**Figure 4-1**).

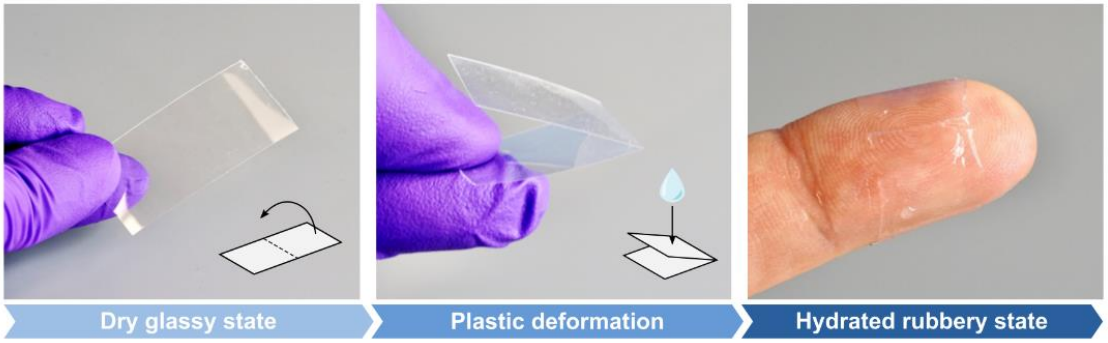

Figure 4-1: Photographs showing the multilayer patch in the plastically-deformable dry glassy state. Upon hydration, the folded patch transitions to the rubbery state and becomes a soft, conformable hydrogel.

4.1.2 Balloon Catheter-based Delivery Method

Balloon catheters have long and widely been used for a broad range of applications in various systems of the body, such as for angioplasty, stent delivery, and balloon occlusion. These devices are well-suited for the endoluminal delivery and precise deployment of medical devices and biomaterials in hollow structures (e.g., trachea, esophagus) and large vessels. To be made compatible with balloon catheter-based delivery, the patch can be folded into a sleeve circumscribing the uninflated balloon with the oil-impinged layer oriented radially outward (**Figure 4-2** and **4-3**). Once positioned at the defect site, inflation of the balloon will drive it to

expand and cause the bioadhesive patch to unfold, making contact with the luminal tissue. The radial pressure exerted by the balloon on the bioadhesive and the tissue triggers the dewetting and adhesion of the bioadhesive, resulting in rapid endoluminal sealing. In a proof-of-concept prototype shown in Figure 4-2a, the bioadhesive patch was folded into a simple tri-faced sleeve for coupling with esophageal and Foley catheters. Alternatively, the sleeve can also take the form of a cylinder with numerous pleated "wings" (**Figure 4-2b**). In order to secure the positioning of the sleeve on the balloon, removable stabilizing elements (e.g., stiffening members which dissolve or fracture upon deployment) can be incorporated which restrict movement, bunching, or rotation during travel through the lumen.

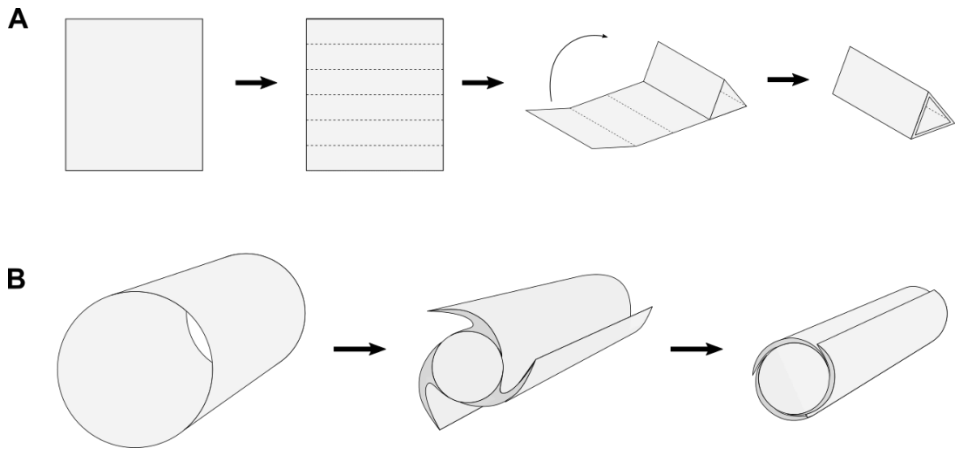

Figure 4-2: Folding schematic for (a) a triangular sleeve and (b) a pleated cylindrical sleeve with "wings" for integration of the bioadhesive patch with a balloon catheter. The numbers of edges and wings may vary.

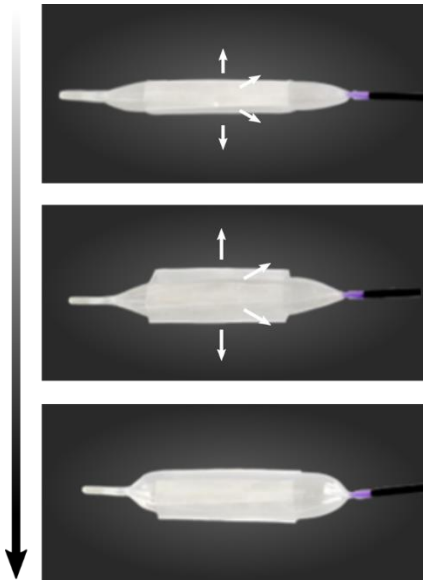

Figure 4-3: Photographs showing the deployment mechanism using an esophageal balloon catheter.

4.1.3 STAPLER-BASED DELIVERY METHOD

A ubiquitous surgical instrument in endoscopic surgery is the articulating stapler, which is designed to cut and seal segments of tissue by clamping the desired tissue site between an anvil and a stapler cartridge, firing parallel lines of staples, and then actuating a blade to cut the tissue in between the two staples lines. While surgical staplers have substantial device failure rates when used to firing staples, the ability to maneuver surgical staplers through small ports and actuate the jaws to lock and apply firm compression provides these devices with versatile utility, including the potential to apply the multilayer patch.

To enable stapler-based minimally invasive delivery, the multilayer patch can be cut into various-sized strips and loaded in a folded origami sleeve designed to wrap around the anvil and cartridge units of the stapler (**Figure 4-4**). Once the stapler jaws are positioned around the site of

the tissue injury, actuation of the stapler compresses the multilayer patches against the tissue surface, triggering adhesion and sealing of the defect (**Figure 4-5**).

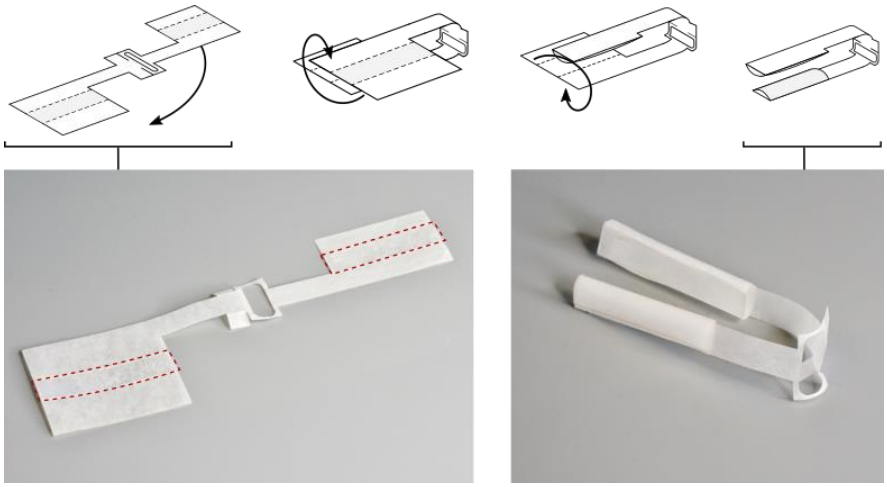

Figure 4-4: Exemplary folding schematic for integration with a surgical stapler.

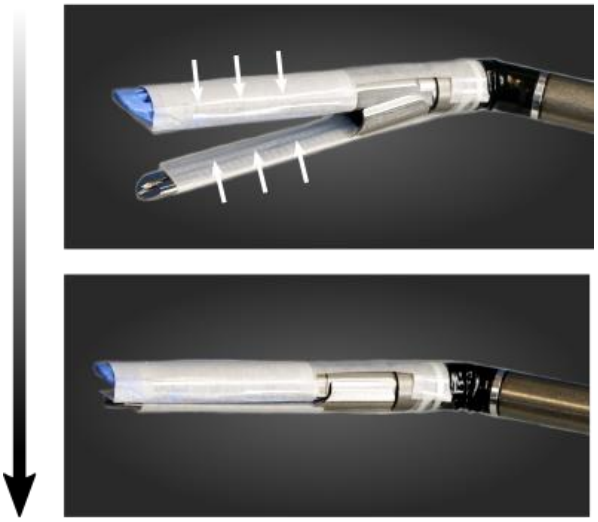

Figure 4-5: Photographs showing the deployment mechanism of an exemplary embodiment using an articulating linear stapler.

4.2 *EX VIVO* DEMONSTRATIONS

To explore the translational potential of the multilayer patch, various proof-of-concept demonstrations using *ex vivo* porcine models were performed according to the two deployment strategies described above: tracheal defect repair, esophageal defect repair, aortic defect repair, and intestinal defect repair (**Figures 4-6** and **4-7**). All ex vivo experiments were reviewed and approved by the Committee on Animal Care at the Massachusetts Institute of Technology. All porcine tissues and organs for ex vivo experiments (skin, trachea, aorta, esophagus, intestine) were purchased from a research-grade porcine tissue vendor (Sierra Medical Inc.).

4.2.1 TRACHEAL DEFECT REPAIR

For the *ex vivo* tracheal defect model, a 5 mm circular transmural defect was created in the wall of a porcine trachea (with intact lungs) using a biopsy punch. The upper portion of the trachea was connected to tubing through which air was pumped to the lung lobes. A multilayer patch was folded into an origami sleeve as described in Section 4.1.2 and fitted with a Foley catheter (ReliaMed). The assembled balloon was inserted into the lumen of the damaged trachea. Once the multilayer patch was located at the position of the defect, the balloon was inflated by introducing air into the catheter. Pressure was held for 5 seconds prior to deflation and removal of the balloon (**Figure 4-6a**). After sealing of the tracheal defect, air was pumped through the trachea to check for the hermetic sealing of the trachea. It was observed that the application and adhesion of the multilayer patch restored the previously compromised inflation capability of the lungs (**Figure 4-6b**).

4.2.2 ESOPHAGEAL DEFECT REPAIR

The esophageal defect repair model was similar to that for tracheal defect repair. Briefly, 5 mm circular transmural defect was punched in the wall of a porcine esophagus with a biopsy punch. Water was flowed through the esophagus using a tubing and a peristaltic pump (Thermo Fisher) to visualize leakage through the defect. A multilayer patch was folded into an origami sleeve and fitted with an esophageal catheter (Boston Scientific), then deployed at the defect site. After sealing of the esophageal defect, water was pumped through the trachea to check the fluid-tight sealing of the esophagus (**Figure 4-6c**). The esophageal seal withstood the pumping of water without leakage at supraphysiological pressures over 300 mm Hg.

4.2.3 AORTIC DEFECT REPAIR

The Foley catheter method described for the treacheal defect repair model was further used to achieve hemostatic sealing in an *ex vivo* aorta. Porcine blood was flowed through the aorta using a tubing and a peristaltic pump (Thermo Fischer) to visualize leakage through the defect (**Figure 4-6d**). As with the esophageal seal, the aortic seal withstood the pumping of water without leakage at supraphysiological pressures over 300 mm Hg. For all endoluminal delivery models, an endoscopic camera (DEPSTECH) was used for visualization.

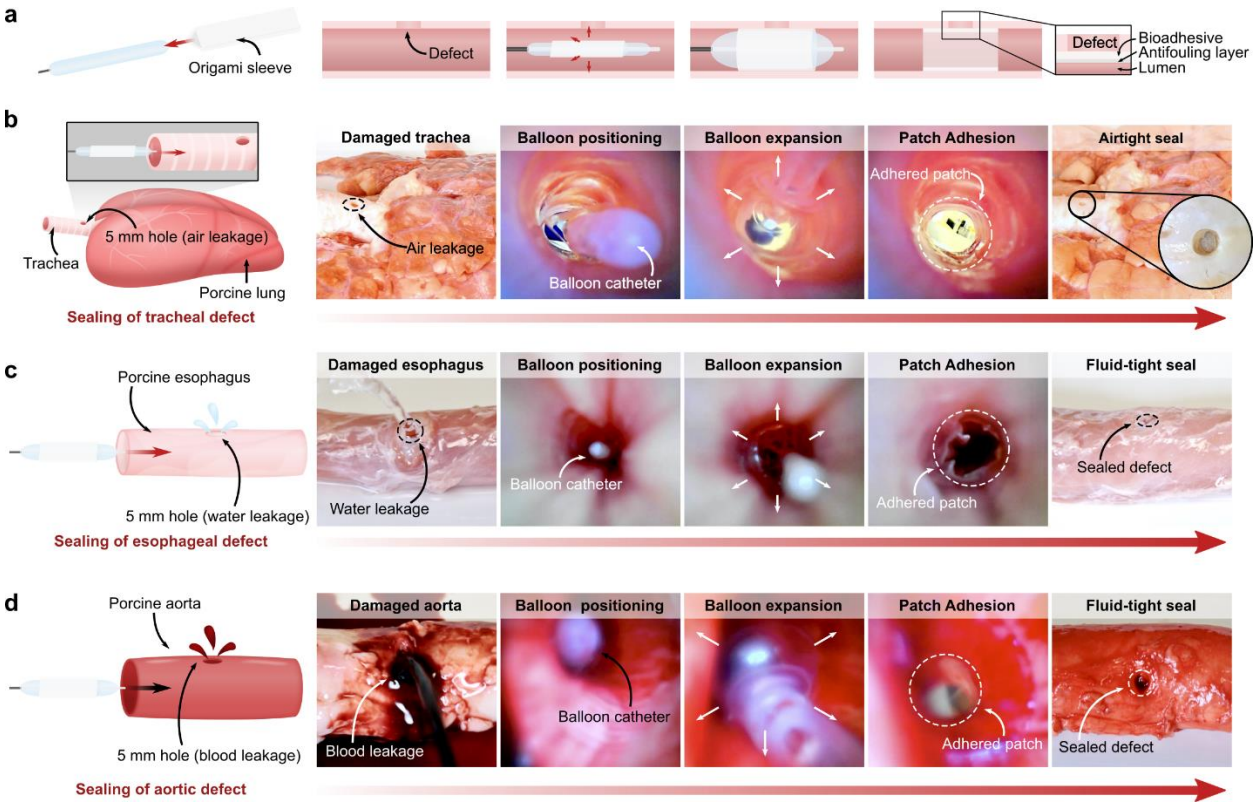

Figure 4-6: *Ex vivo* demonstrations of minimally invasive delivery and application of the multilayer bioadhesive patch by balloon catheters. (a) Schematic illustrations of the origami patch integration and endoluminal delivery process using a balloon catheter. (b) Macroscopic and endoscopic photographs taken during the process of sealing of a porcine tracheal defect, (c) esophageal defect, and (d) aortic defect.

4.2.4 Intestinal Defect Repair

For the intestinal defect repair model, a 5 mm circular defect was created through the walls of a porcine small intestine using a biopsy punch. A patch-loaded origami sleeve was folded and introduced to an articulating linear stapler (Ethicon) according to the design described in Section 4.1.3. The assembled stapler was navigated to the defect site and actuated to apply compression for 5 seconds, before opening the jaws and retracting the stapler (**Figure 4-7a,b**). The repaired

intestine was connected to a pump and inflated to check for fluid-tight sealing of the bowel. To simulate a minimally invasive surgical setting, the experiment was repeated inside a dark chamber with holes, using endoscopic camera footage to guide the process (**Figure 4-7c**). As represented by these ex vivo demonstrations, the multilayer patch can potentially serve as a primary sealing and repair modality for various organ defects. Alternatively, it can act as an adjunct on top of a suture or staple line to support an anastomosis, especially in patients at high risk of anastomotic failure.

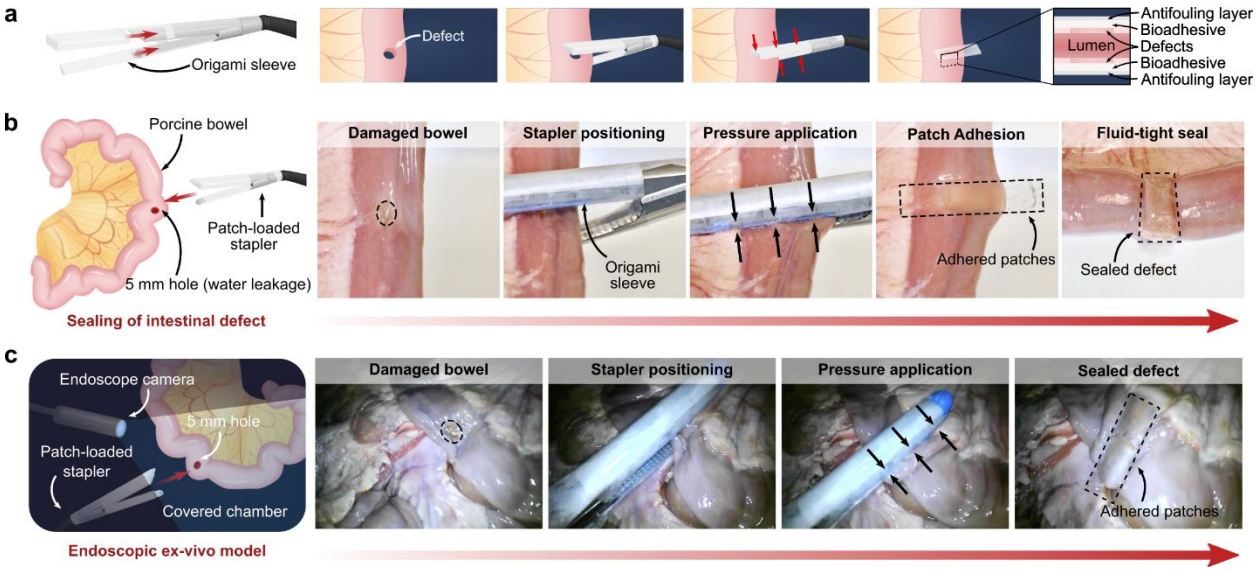

Figure 4-7: *Ex vivo* demonstrations of minimally invasive delivery and application of the multilayer bioadhesive patch using a surgical stapler. **(**a) Schematic illustrations of the patch integration and delivery process using an articulating linear stapler. (b) Macroscopic photographs of the linear sealing of a porcine intestinal defect (c) Endoscopic footage of the sealing of a porcine intestinal performed in a dark, covered chamber to mimic a minimally invasive surgical procedure.

CHAPTER 5

Conclusion and Outlook

In this thesis, the development of a multifunctional patch was described with the principal goal of addressing the multifaceted clinical needs for improved minimally invasive tissue repair techniques. By employing a multilayered architecture comprising various materials and structures, the resulting patch is capable of achieving a wide range of functionalities: (1) fast, robust, and fluid-tight tissue adhesion through adoption of a dry-crosslinking mechanism; (2) resistance to contamination by body fluids through integration of a liquid-infused protective matrix which can be removed under sufficient pressure; and (3) mitigation of post-implantation fouling by bacteria and biomolecules associated with infection, thrombosis, and fibrosis through the creation of a zwitterionic-interpenetrated elastomer. Taking advantage of the material properties and tape-like form factor of the patch, various origami-based manufacturing techniques have been demonstrated which enable the potential application in diverse minimally invasive procedures.

While the experimental characterizations, *ex vivo* demonstrations, and *in vivo* small animal models have thus far shown promising results, more work will need to be done to rigorously investigate the long-term biocompatibility and treatment efficacy of the multilayer patch. Furthermore, the customizability of the patch opens doors to future designs and deployment strategies. Ideally, the form factor, material properties, and constituent layers of the patch should be optimized for each specific clinical indication.

This research has been greatly motivated by the current limitations of existing tissue repair methods. Given the design flexibility and unique capabilities of the multilayer patch, I hope this work will help to form a basis for the future development of materials that have the potential to overcome translational barriers in surgery and facilitate the broader adoption of less damaging and less invasive surgical techniques.

REFERENCES

[1] Z. Wang, X. Dai, H. Xie, J. Feng, Z. Li, and Q. Lu, "The efficacy of staple line reinforcement during laparoscopic sleeve gastrectomy: A meta-analysis of randomized controlled trials," *International Journal of Surgery*, vol. 25, pp. 145–152, Jan. 2016, doi: 10.1016/j.ijsu.2015.12.007.

[2] G. H. Ballantyne, "The pitfalls of laparoscopic surgery: challenges for robotics and telerobotic surgery," *Surg Laparosc Endosc Percutan Tech*, vol. 12, no. 1, pp. 1–5, Feb. 2002, doi: 10.1097/00129689-200202000-00001.

[3] C. for D. and R. Health, "Safe Use of Surgical Staplers and Staples – Letter to Health Care Providers," *FDA*, Dec. 2019, Accessed: Jun. 27, 2020. [Online]. Available: https://www.fda.gov/medical-devices/letters-health-care-providers/safe-use-surgical-staplers-and-staples-letter-health-care-providers

[4] T. B. Reece, T. S. Maxey, and I. L. Kron, "A prospectus on tissue adhesives," *The American Journal of Surgery*, vol. 182, no. 2, pp. S40–S44, Aug. 2001, doi: 10.1016/S0002-9610(01)00742-5.

[5] Z. A. Murrell and M. J. Stamos, "Reoperation for Anastomotic Failure," *Clin Colon Rectal Surg*, vol. 19, no. 4, pp. 213–216, Nov. 2006, doi: 10.1055/s-2006-956442.

[6] D. N. Papachristou and J. G. Fortner, "Anastomotic failure complicating total gastrectomy and esophagogastrectomy for cancer of the stomach," *The American Journal of Surgery*, vol. 138, no. 3, pp. 399–402, Sep. 1979, doi: 10.1016/0002-9610(79)90271-X.

[7] H. Capella-Monsonís, S. Kearns, J. Kelly, and D. I. Zeugolis, "Battling adhesions: from understanding to prevention," *BMC Biomedical Engineering*, vol. 1, no. 1, p. 5, Feb. 2019, doi: 10.1186/s42490-019-0005-0.

[8] "Postoperative adhesion development after operative laparoscopy: evaluation at early second-look procedures**Presented in part at the 46th Annual Meeting of The American Fertility Society, Washington D.C., October 15 to 18, 1990.," *Fertility and Sterility*, vol. 55, no. 4, pp. 700–704, Apr. 1991, doi: 10.1016/S0015-0282(16)54233-2.

[9] K. H. Fuchs, "Minimally invasive surgery," *Endoscopy*, vol. 34, no. 2, pp. 154–159, Feb. 2002, doi: 10.1055/s-2002-19857.

[10] M. J. Mack, "Minimally Invasive and Robotic Surgery," *JAMA*, vol. 285, no. 5, pp. 568–572, Feb. 2001, doi: 10.1001/jama.285.5.568.

[11] B. M. Wolfe, Z. Szabo, M. E. Moran, P. Chan, and J. G. Hunter, "Training for minimally invasive surgery: Need for surgical skills," *Surgical Endoscopy*, vol. 7, no. 2, pp. 93–95, 1993, doi: 10.1007/BF00704386.

[12] N. Tanigawa, "Advantages and Problems with Endoscopic Surgery," vol. 52, no. 5, p. 5, 2009.

[13] "Surgical Robots Market Size, Growth | Global Report, 2026." https://www.fortunebusinessinsights.com/industry-reports/surgical-robots-market-100948 (accessed Apr. 18, 2021).

[14] "Minimally Invasive Surgical Instruments Market Size Report, 2019-2026." https://www.grandviewresearch.com/industry-analysis/minimally-invasive-surgical-instruments-market (accessed Apr. 18, 2021).

[15] S. J. Wu, H. Yuk, J. Wu, C. S. Nabzdyk, and X. Zhao, “A Multifunctional Origami Patch for Minimally Invasive Tissue Sealing,” *Advanced Materials*, vol. 33, no. 11, p. 2007667, 2021, doi: https://doi.org/10.1002/adma.202007667.
[16] V. Bhagat and M. L. Becker, “Degradable Adhesives for Surgery and Tissue Engineering,” *Biomacromolecules*, vol. 18, no. 10, pp. 3009–3039, Oct. 2017, doi: 10.1021/acs.biomac.7b00969.
[17] N. Annabi, K. Yue, A. Tamayol, and A. Khademhosseini, “Elastic sealants for surgical applications,” *European Journal of Pharmaceutics and Biopharmaceutics*, vol. 95, pp. 27–39, Sep. 2015, doi: 10.1016/j.ejpb.2015.05.022.
[18] X. Chen, H. Yuk, J. Wu, C. S. Nabzdyk, and X. Zhao, “Instant tough bioadhesive with triggerable benign detachment,” *PNAS*, Jun. 2020, doi: 10.1073/pnas.2006389117.
[19] H. Yuk *et al.*, “Dry double-sided tape for adhesion of wet tissues and devices,” *Nature*, vol. 575, no. 7781, pp. 169–174, Nov. 2019, doi: 10.1038/s41586-019-1710-5.
[20] S. Nam and D. Mooney, “Polymeric Tissue Adhesives,” *Chem. Rev.*, p. acs.chemrev.0c00798, Jan. 2021, doi: 10.1021/acs.chemrev.0c00798.
[21] “Overcoming the translational barriers of tissue adhesives | Nature Reviews Materials.” https://www.nature.com/articles/s41578-019-0171-7?proof=true (accessed Jun. 24, 2020).
[22] M. Ryou and C. C. Thompson, “Tissue Adhesives: A Review,” *Techniques in Gastrointestinal Endoscopy*, vol. 8, no. 1, pp. 33–37, Jan. 2006, doi: 10.1016/j.tgie.2005.12.007.
[23] J. C. Dumville *et al.*, “Tissue adhesives for closure of surgical incisions,” *Cochrane Database of Systematic Reviews*, no. 11, 2014, doi: 10.1002/14651858.CD004287.pub4.
[24] L. Ninan, R. L. Stroshine, J. J. Wilker, and R. Shi, “Adhesive strength and curing rate of marine mussel protein extracts on porcine small intestinal submucosa,” *Acta Biomater*, vol. 3, no. 5, pp. 687–694, Sep. 2007, doi: 10.1016/j.actbio.2007.02.004.
[25] Q. Guo, J. Chen, J. Wang, H. Zeng, and J. Yu, “Recent progress in synthesis and application of mussel-inspired adhesives,” *Nanoscale*, vol. 12, no. 3, pp. 1307–1324, Jan. 2020, doi: 10.1039/C9NR09780E.
[26] J. Li *et al.*, “Tough adhesives for diverse wet surfaces,” *Science*, vol. 357, no. 6349, pp. 378–381, Jul. 2017, doi: 10.1126/science.aah6362.
[27] N. Lang *et al.*, “A blood-resistant surgical glue for minimally invasive repair of vessels and heart defects,” *Sci Transl Med*, vol. 6, no. 218, p. 218ra6, Jan. 2014, doi: 10.1126/scitranslmed.3006557.
[28] N. Annabi *et al.*, “Engineering a highly elastic human protein–based sealant for surgical applications,” *Science Translational Medicine*, vol. 9, no. 410, Oct. 2017, doi: 10.1126/scitranslmed.aai7466.
[29] A. P. Duarte, J. F. Coelho, J. C. Bordado, M. T. Cidade, and M. H. Gil, “Surgical adhesives: Systematic review of the main types and development forecast,” *Progress in Polymer Science*, vol. 37, no. 8, pp. 1031–1050, Aug. 2012, doi: 10.1016/j.progpolymsci.2011.12.003.
[30] R. D. O’Rorke *et al.*, “Addressing Unmet Clinical Needs with UV Bioadhesives,” *Biomacromolecules*, vol. 18, no. 3, pp. 674–682, Mar. 2017, doi: 10.1021/acs.biomac.6b01743.
[31] “Carbodiimide Crosslinker Chemistry - US.” //www.thermofisher.com/us/en/home/life-science/protein-biology/protein-biology-learning-center/protein-biology-resource-

library/pierce-protein-methods/carbodiimide-crosslinker-chemistry.html (accessed Apr. 20, 2021).
[32] R. C. F. Cheung, T. B. Ng, J. H. Wong, and W. Y. Chan, "Chitosan: An Update on Potential Biomedical and Pharmaceutical Applications," *Mar Drugs*, vol. 13, no. 8, pp. 5156–5186, Aug. 2015, doi: 10.3390/md13085156.
[33] F. Ahmadi, Z. Oveisi, S. M. Samani, and Z. Amoozgar, "Chitosan based hydrogels: characteristics and pharmaceutical applications," *Res Pharm Sci*, vol. 10, no. 1, pp. 1–16, 2015.
[34] H. Yuk, T. Zhang, S. Lin, G. A. Parada, and X. Zhao, "Tough bonding of hydrogels to diverse non-porous surfaces," *Nature Materials*, vol. 15, no. 2, Art. no. 2, Feb. 2016, doi: 10.1038/nmat4463.
[35] W.-S. Kim, I.-H. Yun, J.-J. Lee, and H.-T. Jung, "Evaluation of mechanical interlock effect on adhesion strength of polymer–metal interfaces using micro-patterned surface topography," *International Journal of Adhesion and Adhesives*, vol. 30, no. 6, pp. 408–417, Sep. 2010, doi: 10.1016/j.ijadhadh.2010.05.004.
[36] S. Y. Yang *et al.*, "A bio-inspired swellable microneedle adhesive for mechanical interlocking with tissue," *Nature Communications*, vol. 4, no. 1, Art. no. 1, Apr. 2013, doi: 10.1038/ncomms2715.
[37] S. Yashima, N. Takase, T. Kurokawa, and J. P. Gong, "Friction of hydrogels with controlled surface roughness on solid flat substrates," *Soft Matter*, vol. 10, no. 18, pp. 3192–3199, Apr. 2014, doi: 10.1039/C3SM52883A.
[38] A. K. Epstein, T.-S. Wong, R. A. Belisle, E. M. Boggs, and J. Aizenberg, "Liquid-infused structured surfaces with exceptional anti-biofouling performance," *Proceedings of the National Academy of Sciences*, vol. 109, no. 33, pp. 13182–13187, Aug. 2012, doi: 10.1073/pnas.1201973109.
[39] T.-S. Wong *et al.*, "Bioinspired self-repairing slippery surfaces with pressure-stable omniphobicity," *Nature*, vol. 477, no. 7365, pp. 443–447, Sep. 2011, doi: 10.1038/nature10447.
[40] C. Howell, A. Grinthal, S. Sunny, M. Aizenberg, and J. Aizenberg, "Designing Liquid-Infused Surfaces for Medical Applications: A Review," *Adv. Mater.*, vol. 30, no. 50, p. 1802724, Dec. 2018, doi: 10.1002/adma.201802724.
[41] M. J. Kreder, J. Alvarenga, P. Kim, and J. Aizenberg, "Design of anti-icing surfaces: smooth, textured or slippery?," *Nat Rev Mater*, vol. 1, no. 1, p. 15003, Jan. 2016, doi: 10.1038/natrevmats.2015.3.
[42] M. Villegas, Y. Zhang, N. Abu Jarad, L. Soleymani, and T. F. Didar, "Liquid-Infused Surfaces: A Review of Theory, Design, and Applications," *ACS Nano*, vol. 13, no. 8, pp. 8517–8536, Aug. 2019, doi: 10.1021/acsnano.9b04129.
[43] S. Amini *et al.*, "Preventing mussel adhesion using lubricant-infused materials," *Science*, vol. 357, no. 6352, pp. 668–673, Aug. 2017, doi: 10.1126/science.aai8977.
[44] J. D. Smith *et al.*, "Droplet mobility on lubricant-impregnated surfaces," *Soft Matter*, vol. 9, no. 6, pp. 1772–1780, Jan. 2013, doi: 10.1039/C2SM27032C.
[45] H. F. Bohn and W. Federle, "Insect aquaplaning: Nepenthes pitcher plants capture prey with the peristome, a fully wettable water-lubricated anisotropic surface," *Proc Natl Acad Sci U S A*, vol. 101, no. 39, pp. 14138–14143, Sep. 2004, doi: 10.1073/pnas.0405885101.
[46] F. Barca, T. Caporossi, and S. Rizzo, "Silicone Oil: Different Physical Proprieties and Clinical Applications," *Biomed Res Int*, vol. 2014, 2014, doi: 10.1155/2014/502143.

[47] K. R. Langley and S. T. Thoroddsen, “Gliding on a layer of air: impact of a large-viscosity drop on a liquid film,” *Journal of Fluid Mechanics*, vol. 878, Nov. 2019, doi: 10.1017/jfm.2019.682.
[48] D. J. Walls, E. Meiburg, and G. G. Fuller, “The shape evolution of liquid droplets in miscible environments,” *Journal of Fluid Mechanics*, vol. 852, pp. 422–452, Oct. 2018, doi: 10.1017/jfm.2018.535.
[49] J. B. Boreyko, G. Polizos, P. G. Datskos, S. A. Sarles, and C. P. Collier, “Air-stable droplet interface bilayers on oil-infused surfaces,” *PNAS*, vol. 111, no. 21, pp. 7588–7593, May 2014, doi: 10.1073/pnas.1400381111.
[50] H. Yuk *et al.*, “Barnacle-Inspired Paste for Instant Hemostatic Tissue Sealing,” Bioengineering, preprint, Dec. 2020. doi: 10.1101/2020.12.12.422505.
[51] O. Reynolds, “On the Theory of Lubrication and Its Application to Mr. Beauchamp Tower’s Experiments, Including an Experimental Determination of the Viscosity of Olive Oil,” *Philosophical Transactions of the Royal Society of London*, vol. 177, pp. 157–234, 1886.
[52] B. N. J. Persson, A. I. Volokitin, and E. Tosatti, “Role of the external pressure on the dewetting of soft interfaces,” *Eur. Phys. J. E*, vol. 11, no. 4, pp. 409–413, Aug. 2003, doi: 10.1140/epje/i2003-10054-2.
[53] W. Hutt and B. N. J. Persson, “Soft matter dynamics: Accelerated fluid squeeze-out during slip,” *J. Chem. Phys.*, vol. 144, no. 12, p. 124903, Mar. 2016, doi: 10.1063/1.4944384.
[54] B. N. J. Persson *et al.*, “Elastic contact mechanics: Percolation of the contact area and fluid squeeze-out,” *Eur. Phys. J. E*, vol. 35, no. 1, p. 5, Jan. 2012, doi: 10.1140/epje/i2012-12005-2.
[55] G. Carbone and B. Persson, “Dewetting at soft viscoelastic interfaces,” *The Journal of chemical physics*, vol. 121, pp. 2246–52, Sep. 2004, doi: 10.1063/1.1768156.
[56] B. Lorenz and B. Persson, “Fluid squeeze-out between rough surfaces: Comparison of theory with experiment,” *Journal of physics. Condensed matter : an Institute of Physics journal*, vol. 23, p. 355005, Sep. 2011, doi: 10.1088/0953-8984/23/35/355005.
[57] R. B. Woodward and C. H. Schramm, “SYNTHESIS OF PROTEIN ANALOGS,” *J. Am. Chem. Soc.*, vol. 69, no. 6, pp. 1551–1552, Jun. 1947, doi: 10.1021/ja01198a526.
[58] L. Zheng, H. S. Sundaram, Z. Wei, C. Li, and Z. Yuan, “Applications of zwitterionic polymers,” *Reactive and Functional Polymers*, vol. 118, pp. 51–61, Sep. 2017, doi: 10.1016/j.reactfunctpolym.2017.07.006.
[59] L. Carr, G. Cheng, H. Xue, and S. Jiang, “Engineering the Polymer Backbone To Strengthen Nonfouling Sulfobetaine Hydrogels,” *Langmuir*, vol. 26, no. 18, pp. 14793–14798, Sep. 2010, doi: 10.1021/la1028004.
[60] W.-W. Yue, H.-J. Li, T. Xiang, H. Qin, S.-D. Sun, and C.-S. Zhao, “Grafting of zwitterion from polysulfone membrane via surface-initiated ATRP with enhanced antifouling property and biocompatibility,” *Journal of Membrane Science*, vol. 446, pp. 79–91, Nov. 2013, doi: 10.1016/j.memsci.2013.06.029.
[61] J. Wu, W. Lin, Z. Wang, S. Chen, and Y. Chang, “Investigation of the Hydration of Nonfouling Material Poly(sulfobetaine methacrylate) by Low-Field Nuclear Magnetic Resonance,” *Langmuir*, vol. 28, no. 19, pp. 7436–7441, May 2012, doi: 10.1021/la300394c.

[62] Q. Shao and S. Jiang, “Molecular Understanding and Design of Zwitterionic Materials,” *Advanced Materials*, vol. 27, no. 1, pp. 15–26, 2015, doi: https://doi.org/10.1002/adma.201404059.
[63] S. Jiang and Z. Cao, “Ultralow-Fouling, Functionalizable, and Hydrolyzable Zwitterionic Materials and Their Derivatives for Biological Applications,” *Advanced Materials*, vol. 22, no. 9, pp. 920–932, 2010, doi: 10.1002/adma.200901407.
[64] H. He *et al.*, “Zwitterionic poly(sulfobetaine methacrylate) hydrogels with optimal mechanical properties for improving wound healing in vivo,” *J. Mater. Chem. B*, vol. 7, no. 10, pp. 1697–1707, Mar. 2019, doi: 10.1039/C8TB02590H.
[65] Y. Iwasaki, K. Shimakata, N. Morimoto, and K. Kurita, “Hydrogel-like elastic membrane consisting of semi-interpenetrating polymer networks based on a phosphorylcholine polymer and a segmented polyurethane,” *Journal of Polymer Science Part A: Polymer Chemistry*, vol. 41, no. 1, pp. 68–75, 2003, doi: https://doi.org/10.1002/pola.10554.
[66] Z. Zhang, T. Chao, and S. Jiang, “Physical, Chemical, and Chemical−Physical Double Network of Zwitterionic Hydrogels,” *J. Phys. Chem. B*, vol. 112, no. 17, pp. 5327–5332, May 2008, doi: 10.1021/jp710683w.
[67] L. P. Kreuzer *et al.*, “Swelling and Exchange Behavior of Poly(sulfobetaine)-Based Block Copolymer Thin Films,” *Macromolecules*, vol. 52, no. 9, pp. 3486–3498, May 2019, doi: 10.1021/acs.macromol.9b00443.
[68] J. Ning, G. Li, and K. Haraguchi, “Synthesis of Highly Stretchable, Mechanically Tough, Zwitterionic Sulfobetaine Nanocomposite Gels with Controlled Thermosensitivities,” *Macromolecules*, vol. 46, no. 13, pp. 5317–5328, Jul. 2013, doi: 10.1021/ma4009059.
[69] L. Chen, J. Gong, and Y. Osada, “Novel Thermosensitive IPN Hydrogel Having a Phase Transition Without Volume Change,” *Macromolecular Rapid Communications*, vol. 23, no. 3, pp. 171–174, 2002, doi: https://doi.org/10.1002/1521-3927(20020201)23:3<171::AID-MARC171>3.0.CO;2-P.
[70] W. Wang, “Polyurethane for biomedical applications: A review of recent developments,” *The design and manufacture of medical devices*, p. 37.
[71] Y. Yu *et al.*, “Multifunctional ‘Hydrogel Skins’ on Diverse Polymers with Arbitrary Shapes,” *Advanced Materials*, vol. 31, no. 7, p. 1807101, Feb. 2019, doi: 10.1002/adma.201807101.
[72] D. C. Leslie *et al.*, “A bioinspired omniphobic surface coating on medical devices prevents thrombosis and biofouling,” *Nat Biotechnol*, vol. 32, no. 11, pp. 1134–1140, Nov. 2014, doi: 10.1038/nbt.3020.